UNIVERSITY OF CALIFORNIA SAN DIEGO

Wired to Fire: Electric Signaling in Biofilms and Spores

A dissertation submitted in partial satisfaction of the
requirements for the degree
Doctor of Philosophy

in

Biology with a Specialization in Quantitative Biology

by

Kaito Kikuchi

Committee in charge:

Professor Gürol Mehmet Süel, Chair
Professor Terence T. Hwa
Professor Gulcin Pekkurnaz
Professor Joseph A. Pogliano
Professor Faik Akif Tezcan

2022

The dissertation of Kaito Kikuchi is approved, and it is acceptable in quality and form for publication on microfilm and electronically.

University of California San Diego

2022

DEDICATION

To my *Ojīchan*, Daizo Kikuchi.

TABLE OF CONTENTS

LIST OF FIGURES

LIST OF TABLES

ACKNOWLEDGEMENTS

First, I thank my thesis advisor, Gürol Süel, for his mentorship during my 6 years in his lab. His unparalleled knack for scientific storytelling drew me to his lab in the first place, and I am grateful for his guidance on how to structure talks and papers, as well as maintaining a tight-knit research group. I also thank my thesis committee members; Terry Hwa, Gulcin Pekkurnaz, Joe Pogliano, and Akif Tezcan, for their constructive and friendly feedback, and for always, eventually, being available to meet.

Joe Larkin has been an amazing mentor and friend in the lab. I remember our first conversation, which happened to be about ethnic minorities in Japan: I was blown away that someone knew about the Ainu. I quickly befriended this trivia grandmaster, who was always extraordinarily generous with his time and would help me inside and outside the lab countless times while remembering to impart some quirky tidbit about the Frisian language. I am sure that his new lab would prove to be a fertile well of scientific discoveries that run as deep as his knowledge and generosity.

Leticia Galera-Laporta has also been a dear friend in the lab. I would not have been able to come this far in our spore project if not for her relentless optimism and unmatched work ethic, and I am forever honored to have her as my co-first author. I enjoyed our hangouts in both her native Barcelona and in our home-away-from-home San Diego, and occasionally incurring her fierce competitive wrath over board games.

The past six years in San Diego was a blast thanks to my excellent friends in the Biological Sciences PhD program. I especially appreciate my cabal of cohort mates: Sam Redford for his kindness and shared enthusiasm in beer and pottery, Al Romero for her reliable chaos and surf coaching, Bianca Barriga for our gourmet Sunday dinners, Jenny He for her hot pot parties and being the chill responsible adult, and Abby Gillespie for regaling her many adventures and cat sitting Uri. I also wish to thank members of the Süel lab past and present: every one of you were pleasant to work with and to share the ups and downs of research life. Special credit is due to

Colleen Weatherwax for being the authoritative source of the dankest memes.

Finally I wish to thank my family, who were always there to support me during my academic journey. My parents opened the door to the world by enrolling me in an international school in Hong Kong, allowing me to grow up bilingual in Japanese and English. My grandparents on both sides of the family have also always encouraged my studies, and I was able to weather the inevitable moments of doubt by reminding myself of their unconditional happiness in my being. Last but not least, I thank my husband Blake, for being the bottomless source of warmth that nourishes my soul.

Chapter 2, in full, is a reprint of the material as it appears in Larkin JW, Zhai X, Kikuchi K, Redford SE, Prindle A, Liu J, Greenfield S, Walczak AM, Garcia-Ojalvo J, Mugler A, Süel GM,"Signal percolation within a bacterial community", *Cell Systems*, 2018. The dissertation author was a co-author of this paper. We acknowledge Massimo Vergassola, Munehiro Asally, Steve Lockless, Tolga Çağatay, Lev Tsimring, Terry Hwa, Uri Alon, and Michael Elowitz for helpful discussions. We acknowledge Dong-yeon D. Lee for assistance during strain construction.

Chapter 3 is currently under review in the working citation: Kikuchi K, Galera-Laporta L, Weatherwax C, Lam JY, Moon E, Theodorakis EA, Garcia-Ojalvo J, Süel GM,"Electrochemical potential enables dormant spores to integrate environmental signals". The dissertation author was a primary investigator and the first author of this material alongside Leticia Galera-Laporta. We acknowledge Munehiro Asally, Tolga Çağatay, Joseph Larkin, Colin Comerci, and Katherine Süel for helpful discussions; Wade Winkler and David Kearns for kindly providing bacterial strains; and Jacqueline Humphries for help with strain construction.

VITA

2014	B. A. in Biology, International Christian University
2016	M. A. in Biophysics, University of Tokyo
2022	Ph. D. in Biology with a Specialization in Quantitative Biology, University of California San Diego

PUBLICATIONS

Kikuchi K, Galera-Laporta L, Weatherwax C, Lam JY, Moon E, Theodorakis EA, Garcia-Ojalvo J, Süel GM,"Electrochemical potential enables dormant spores to integrate environmental signals", *under review*.

Zhai X, Larkin JW, **Kikuchi K**, Redford SE, Roy U, Süel GM, Mugler A, "Statistics of correlated percolation in a bacterial community", *PLoS Computational Biology*, 2019.

Larkin JW, Zhai X, **Kikuchi K**, Redford SE, Prindle A, Liu J, Greenfield S, Walczak AM, Garcia-Ojalvo J, Mugler A, Süel GM,"Signal percolation within a bacterial community", *Cell Systems*, 2018.

Hill SM, Heiser LM, Cokelaer T, Unger M, Nesser NK, Carlin DE, Zhang Y, Sokolov A, Paull EO, Wong CK, Graim K, Bivol A, Wang A, Zhu F, Afsari B, Danilova LV, Favorov AV, Lee WS, Taylor D, Hu CW, Long BL, Noren DP, Bisberg AJ, The HPN-DREAM Consortium (including **Kikuchi K**), Mills GB, Gray JW, Kellen M, Norman T, Friend S, Qutub AA, Fertig EJ, Guan Y, Song M, Stuart JM, Spellman PT, Koeppl H, Stolovitzky G, Saez-Rodriguez J, Mukherjee S, "Inferring causal molecular networks: empirical assessment through a community-based effort", *Nature Methods*, 2016.

Hase T, **Kikuchi K**, Ghosh S, Kitano H, Tanaka H, "Identification of drug-target modules in the human protein-protein interaction network", *Artificial Life and Robotics*, 2014.

ABSTRACT OF THE DISSERTATION

Wired to Fire: Electric Signaling in Biofilms and Spores

by

Kaito Kikuchi

Doctor of Philosophy in Biology with a Specialization in Quantitative Biology

University of California San Diego, 2022

Professor Gürol Mehmet Süel, Chair

Cells, the fundamental unit of life, exist in an ever-changing environment. The ability to sense the environment and decide on a suitable strategy is therefore one of the most important cellular functions. In this dissertation, I will describe two examples of signal transmission and processing that utilize ions. In Chapter 2, I will demonstrate how *Bacillus subtilis* cells self-organize to optimize longe-range signal transmission, in a striking example of statistical physics informing multilevel cellular behavior. In Chapter 3, I will show how *B. subtilis* spores use stored ions to integrate external signals to decide whether to revive from dormancy. Taken together, these examples show the integral role of ions in biological signaling: weaving communication wires that span thousands of cells, and working to reignite life from a complete stop.

Chapter 1

Introduction

1.1 Cells as a unit of signal transmission and processing

Cells, whether in isolation in the wild or embedded within our bodies, reside in dynamic environments with constantly shifting landscapes of nutrient availability and different stress sources. This makes it important to have a sophisticated array of sensory mechanisms as well as mechanisms that enable cells to evaluate sensory information and choose the best way to cope with the environment. For example, bacterial cells are able to sense the gradient of nutrient concentrations as they swim through liquid and move towards the source by changing how their molecular propellers (flagella) rotate. This process, known as chemotaxis, is a classic example of dynamic cellular decision making that integrates external information and translates that into cellular behavior. While cellular motility is by nature a string of highly transient decisions, other decisions such as those that involve cell-fate differentiation would be harder (if not impossible) to reverse, and therefore the decision making process there will need to be made carefully. Furthermore, signal transmission and processing does not come free, as like any cellular process, they would also have to be budgeted from a finite supply of energy. Biologists have uncovered many strategies that cells and organisms take in order to maximize fitness (likelihood of growth

or retaining progeny) in face of uncertain futures and biological costs.

1.2 Communication is key to decision making

Any well-informed decision, as the term suggests, needs information. In the case of cells, this information may come in the form of external signals such as the presence of nutrients or stress, or internal signals such as cell volume or DNA replication errors. In one particularly important avenue, cell-to-cell communication, cells themselves relay signals to each other for collective behavior. Organismal biology is full of such communications and are essential to developing and maintaining a healthy cellular and organismal state.

Bacteria often form complex multicellular communities named biofilms. Biofilms function like a multicellular organism in the sense that individual cells benefit from collective protection from external threats, as well as providing common goods or value in the form of division-of-labor. As expected, biofilms also are prime examples of cell-to-cell communication influencing cellular decisions. For instance, a growing biofilm needs to balance growth with nutrient supply in order to keep the whole community healthy. In absence of a resource management mechanism, cells located in peripheral regions with ample contact with external nutrients may gobble up all the food, leaving cells in the interior of the biofilm to starve. *Bacillus subtilis* biofilms solve this problem by cell-to-cell communication. When cells in the interior regions sense nutrient starvation, they open potassium ion channels in their membranes to release intracellular potassium. This sudden increase in local extracellular potassium ions depolarize neighboring cells, which induce growth arrest and subsequent potassium release. This continues throughout the biofilm in a bucket-brigade fashion all the way to the periphery, halting cell growth to allow nutrients to diffuse into the biofilm, replenishing supply throughout the community. The process repeats itself when peripheral growth restarts and the internal cells starve, leading to a characteristic oscillatory growth behavior [1, 2].

At the single-cell level, there is a further level of cellular decision making involved in this form of electric signaling. Each individual cell balances the cost (growth arrest during signaling) and benefit (health of the community). One extreme scenario would be every cell participating in the signaling process, which would ensure full signal transmission at the cost of full growth arrest. The other extreme would be zero participation, which would have obvious detrimental effects to biofilm health. As such, biofilms need to situate themselves somewhere between these extremes to achieve their objective of full connection without incurring unnecessarily large cost.

In Chapter 2, I will address this process by combining experimental microbiology with statistical physics. By observing signaling biofilms at single-cell resolution, we first noticed that not all of the cells were participating in the process, and that those that participate seemed to be organized in space in a connected network-like structure. Percolation theory, which is a model from statistical physics that describes signal transmission through spatial organization, allowed us to explain how the biofilm balances the cost and benefit of electrical signaling by having a statistically optimal fraction of the cells to participate, ensuring a connected signalling path without unnecessary bloat.

1.3 How to wake up when you're a rock

In face of uncertain environmental outcomes, cell populations often resort to maximizing the fitness of the group as a whole, by diversifying the cell fates that individual cells differentiate into, in effect spreading their bets on hitting the correct strategy that matches the environment. One classic example is the decision making around forming spores in Bacillus subtilis communities. Spores are specialized cell structures that encapsulate a copy of the genome in many layers of protective layers designed to withstand extreme stress. Spore-forming bacteria such as *B. subtilis* generate spores in response to starvation to function as a seed, from which future generations of the cell can revive in case nutritional availability increases. Dormant spores do not grow (or

have any measurable metabolic activities), therefore they carry a large fitness cost to the cell that creates them. This creates a dilemma for the cells: if the environmental downturn is temporary, creating a spore would be unnecessarily costly with minimal gain, but if the nutrient scarcity persists, then all non-spore states will eventually perish, leaving the population to go extinct. *B. subtilis* solves this problem by bet-hedging, committing only a fraction of cells to sporulation, almost as a backup strategy, as the rest of the population continues vegetative growth or alternative and less costly coping strategies such as temporary differentiation into competency (enabling external DNA uptake to potentially gain novel genetic functions).

Of course, as the spore needs to function as a seed, the decision to cease being a spore is as important as the decision to become. The process of spore germination, or more broadly, revival, is a fascinating sequence of events that lead from metabolic death to dynamic growth. In this process, spores rehydrate, remodel their cell wall, repair DNA, and restart macromolecular synthesis. However, one question remains to be answered: how does a metabolically dead spore decide to start this process? *How does a rock think?*

In Chapter 3, I will describe my findings in how *B. subtilis* spores use stored ions to integrate external signals and make decisions during complete dormancy. By combining genetic mutants, chemical perturbations, mathematical modeling, and fluorescence microscopy, we discovered that spores release potassium ions in response to external stimuli, which in turn causes a shift in the electrochemical potential. This moves the dormant spore towards a threshold that, once crossed, starts the irreversible germination program towards complete metabolic revival.

Chapter 2

Signal Percolation within a Bacterial Community

2.1 Abstract

Signal transmission among cells enables long-range coordination in biological systems. However, the scarcity of quantitative measurements hinders the development of theories that relate signal propagation to cellular heterogeneity and spatial organization. We address this problem in a bacterial community that employs electrochemical cell-to-cell communication. We developed a model based on percolation theory, which describes how signals propagate through a heterogeneous medium. Our model predicts that signal transmission becomes possible when the community is organized near a critical phase transition between a disconnected and a fully connected conduit of signaling cells. By measuring population-level signal transmission with single-cell resolution in wild-type and genetically modified communities, we confirm that the spatial distribution of signaling cells is organized at the predicted phase transition. Our findings suggest that at this critical point, the population-level benefit of signal transmission outweighs the single-cell level cost. The bacterial community thus appears to be organized according to a theoretically predicted spatial heterogeneity that promotes efficient signal transmission.

2.2 Introduction

Biological systems, such as tissues or bacterial communities, often require reliable signal transmission among cells to coordinate actions at a distance [3, 4]. In metazoans, highly specialized and sophisticated structures are dedicated to signal transmission, such as axons that relay electrical signals in the nervous system. Densely packed bacterial communities have also been shown to benefit from coordinating their metabolic activities over long distances (exceeding hundreds of cell lengths) to cope with nutrient competition [1, 5]. However, these bacterial communities face at least two major challenges to coordinate cellular actions at long distances. First, it is unclear how bacterial communities can achieve reliable signal propagation to desired target sites without specialized structures that direct the signals. Second, bacterial communities exhibit significant cell-to-cell heterogeneity that can constitute a key obstacle for long-range signal propagation [6, 7, 8]. For example, if only a fraction of cells contributes to signal transmission, the resulting cell-to-cell heterogeneity could cause the propagating signal to die out before reaching its desired target [9, 10, 11, 12]. It is thus important to establish the relevance of heterogeneity in bacterial communities in the context of long-range signal transmission (Fig. 2.1A). The molecular mechanism that underlies signal propagation from the interior of a Bacillus subtilis community toward its edge is based on ion channel-mediated electrochemical cell-to-cell signaling (Fig. 2.1A). Specifically, electrochemical signaling is initiated by cells in the biofilm interior when they experience glutamate starvation during biofilm expansion. This nutrient starvation leads to the opening of the metabolically gated YugO potassium ion channel and subsequent release of intracellular potassium. The resulting local increase in extracellular potassium causes immediately adjacent cells to depolarize, which interferes with their uptake of glutamate, a charged amino acid. Consequently, the depolarized neighboring cell also experiences glutamate limitation and opens its potassium ion channels, releasing its own potassium ions [2]. This cell-to-cell relay mechanism gives rise to a chain reaction that propagates the signal to the biofilm periphery. When

the electrochemical signal reaches the biofilm edge, it halts growth of peripheral cells and thereby reduces their nutrient consumption. This reduction in nutrient consumption allows higher nutrient availability to the stressed cells in the biofilm interior.

When nutrient stress in the interior is alleviated, signaling ceases. Now the biofilm resumes growth, which again results in a renewed starvation of interior cells and initiation of the electrochemical signal. This signaling process thus increases the overall fitness of the biofilm against chemical attack by maintaining a viable population of sheltered interior cells. In addition to the population-level benefit, electrochemical signaling carries a measurable cost to individual cells, in the form of a reduction in growth rate (Fig. 2.1B) [1]. This trade-off between single-cell-level cost and population level benefit suggests that it might be advantageous for the biofilm that not all cells carry the burden of relaying the signal for long-range transmission to succeed. But it is unclear what fraction of signaling cells is needed and how these cells would be organized in space to transmit the signal. Notably, signal propagation through such inhomogeneous populations is not a problem exclusive to biological systems, but a general question that has been deeply explored in fields such as physics, chemistry, and materials science [13, 14, 15]. Percolation theory has emerged as the simplest statistical physics approach that directly addresses this problem. This theory has been commonly applied to study signal propagation through various spatially extended heterogeneous systems [16, 17]. In particular, it describes the emergence of a connected path (connected cluster of cells) that spans the entire size of a spatially extended system, providing a conduit for signal transmission.

Here, we apply the framework of percolation theory to understand how electrochemical signals are propagated across a heterogeneous B. subtilis biofilm community. By incorporating excitable dynamics into a percolation model, we predict the ability of a biofilm to transmit a signal given different fractions of cells participating in signaling, as well as different signaling dynamics. We define cost and benefit for each set of signaling parameters and predict a region in parameter space, determined by the critical percolation point, where the signaling benefit outweighs the

associated cost. Integration of mathematical predictions with quantitative experimental data from wild-type and mutant biofilms suggests that wild-type biofilms operate near this region. Our findings are likely to apply to other percolation systems where the benefit exhibits a sharp sigmoidal shape due to its population-level character, while the cost is associated with the individual units that comprise the system and thus increases linearly with the fraction of signaling units. We argue that in such systems, the benefit will outweigh the cost near the percolation threshold.

2.3 Results

To address the problem of long-range signal transmission in biofilms, we began by constructing a percolation-theory-based model to investigate how a population of cells with heterogeneous electrical activity can reliably propagate signals (Fig. 2.1A, Methods). Percolation theory predicts the transition of a network from having only localized short-range connections to the emergence of a fully connected path that spans the entire system (Fig. 2.1C). Specifically, for a defined two-dimensional lattice, the onset of percolation occurs when the fraction of randomly positioned firing cells, ϕ, reaches a critical value, ϕ_c [18]. At this point, the system undergoes a sharp phase transition in its connectivity, giving rise to a connected cluster of firing cells with a size close to that of the entire system. Below the critical ϕ, too few cells are firing to have sufficient adjacent cells to comprise a fully connected cluster that can span the entire size of the system. Therefore, the probability of having a fully connected conduit for signal transmission across the system remains zero below the critical fraction, but then suddenly jumps to 1 (complete connectivity) as ϕ reaches the critical value. In other words, only when ϕ has reached the critical fraction of firing cells can there be clusters of firing cells that are large enough to span the system. This gives rise to the characteristic sudden phase transitions associated with criticality (Fig. 2.1G) [18].

Given the experimentally constrained size of the system and a modal value of six neighbors for the biofilm cells (Fig. 2.1D), the model predicts an onset of signaling connectivity (percolation) when the fraction of firing cells in the biofilm reaches 0.45 (Figs. 2.1E–G, see Fig. S2.1C for lattices with different numbers of nearest neighbors). At this critical fraction, a firing cell is likely to have at least one immediately adjacent neighbor that is also a firing cell. Consequently, the cluster size distribution of firing cells will have a long tail. In other words, there is always a finite probability of finding a very large, system-spanning cluster of firing cells. Specifically, theory predicts that near this critical percolation threshold, and only near this point, the distribution

of cluster sizes formed by signaling cells follows a power-law decay with an exponent of 2.05 [18](Figs. 2.1H and S2.2). While the critical value for the fraction of firing cells depends on the specifics of the lattice, such as the number of neighboring cells, the exponent is universal (Fig. S2.1D). This means that the exponent value is the same for any two-dimensional lattice and thus a very stringent and general prediction [19].

To reiterate, percolation theory thus makes two precise predictions required for signal transmission to become possible in bacterial communities: (1) the fraction of firing cells in the biofilm should be at, or above, the critical percolation threshold of 0.45, and (2) near the percolation threshold, the distribution of cluster sizes formed by firing cells should follow a power-law decay with a slope of 2.05.

To test these theoretical predictions, we determined the spatial arrangement of signaling cells within biofilms. We utilized a microfluidic platform to grow B. subtilis biofilm communities [1] and image them with single-cell resolution (Fig. S2.3). The microfluidic growth chamber contained designated regions where the biofilm was constrained in height to a two-dimensional monolayer. This allowed us to accurately quantify the spatial organization and dynamics of electrochemical signaling at the single-cell level. Furthermore, the two-dimensional geometry allowed us to directly investigate signal transmission in a geometry where the number of neighboring cells is limited, compared with three-dimensional regions of the biofilm where each cell has more than six neighbors on average. The ability of the biofilm to transmit signals even in a monolayer is crucial, since the leading edge of the biofilm is predominantly a monolayer [20] and constitutes the destination for electrochemical signaling (Fig. 2.2A).

To measure membrane potential of individual bacteria within biofilms during electrochemical signaling, we used the previously characterized fluorescent reporter thioflavin-T (ThT), which acts as a Nernstian membrane potential indicator [2]. Specifically, the higher the membrane potential of the cell, the larger the amplitude of the fluorescent ThT signal. Single-cell resolution measurements of the biofilm show that only some cells exhibit pulses in electrical activity, while

others do not appear to participate in signaling (Figs. 2.2A,B, andS2.4). Analysis of all cells reveals a bimodal distribution of membrane potential amplitudes during signal propagation, with the fraction of signaling cells being $\phi = 0.43 \pm 0.02$ (Fig. 2.2B, Methods), in agreement with the theoretically predicted percolation threshold. We then measured the spatial distribution of signaling (firing) cells and determined that they were clustered in space (Fig. 2.2C). Moreover, the distribution of cluster sizes follows a power-law decay that extends across three decades and has an exponent of approximately 2 (Fig. 2.2D). Both the fraction of firing cells and the distribution of firing cell cluster sizes are thus consistent with percolation theory predictions. These results suggest that the spatial organization of signaling cells within the bacterial community may be organized near the percolation threshold.

Signal transmission is an inherently dynamic process that unfolds over time. In our system, the signal propagates from one cell to the next, where each cell undergoes an excitable pulse (firing) in its membrane potential. The amplitude of the pulse must be sufficiently high to trigger a response in the neighboring cell. It is also important that the cell does not spend excessive time in the firing (and thus non-growing) state, as this would result in unnecessary cost (Fig. 2.1B). In its simplest form, percolation theory is a statistical framework that does not account for such pulse durations and signaling dynamics of cells. Therefore, we created a model that takes into account both the spatial arrangement of firing cells and the single-cell dynamics during signal transmission.

We described the electrochemical signals in the biofilm with the FitzHugh-Nagumo (FN) model of excitable dynamics (Fig. 2.3A) [21]. This simple model, commonly used for studying action potential dynamics in neurons, accounts here for excitable dynamics in individual cells as well as for the transmission of signals between neighboring cells (Figs. 2.3B,C). It contains three parameters: the first is the activation or firing threshold, u_0, which defines the amplitude that an external signal has to exceed in order to trigger a response in the form of a pulse. The second parameter is the recovery time, τ, which sets the pulse duration of a given response and

thus governs the signaling dynamics. The third parameter is the ratio ε of excitation to cell-to-cell coupling strength, which when sufficiently high supports pulse-coupled wave propagation (see Methods)(Mirollo and Strogatz, 1990). To account for heterogeneity in signaling, different fractions of cells can be assigned as firing cells by giving them a higher value for τ than the other cells (Fig. 2.3D). We integrated the FN model with percolation theory by evolving the dynamics on a twodimensional lattice of excitable cells. Simulations show that successful signal propagation through the lattice of cells depends on both the firing duration and the fraction of firing cells. Importantly, for the same dynamic parameters, a fraction of firing cells near or above the percolation threshold enables successful signal transmission, while a fraction below the threshold fails to propagate the signal (Figs. 2.3D,E).

To experimentally investigate how biofilm dynamics and spatial structure jointly determine signal transmission and to integrate our findings with mathematical predictions, we utilized three gene-deletion strains that generate biofilms with altered structure and dynamics (Fig. 2.4A, Methods). We first focused on structural differences among biofilms and began by investigating the Δ*trkA* strain, which lacks the TrkA gating domain of the YugO potassium ion channel and is known to be deficient in electrochemical signaling (Humphries et al., 2017; Liu et al., 2017; Prindle et al., 2015). Indeed, biofilms formed by the Δ*trkA* strain contain a low fraction of firing cells, 0.13 ± 0.04 (mean $\pm$ SEM), compared with 0.43 ± 0.02 observed in wild-type biofilms (Figs. 2.4B,D). We also utilized a strain that lacks the KtrA potassium pump (Δ*ktrA*) and generates biofilms with a fraction of firing cells similar to wild-type biofilms (0.48 ± 0.11). In contrast, deletion of SinR (Δ*sinR*), a transcription factor that represses expression of the YugO ion channel [22], results in biofilms with a higher fraction of firing cells, 0.74 ± 0.04 (Figs. 2.4B,D). Biofilms formed by these strains thus contain structural differences as defined by differences in the fraction of firing cells.

To characterize the signaling dynamics of each strain, we tracked hundreds of individual cells within the wild-type and genetically modified biofilms and measured their electrical activity

during signal transmission (Fig. 2.4C). We found that the wild-type biofilm has the shortest pulse duration, followed by Δ*sinR* and Δ*trkA* biofilms (Fig. 2.4E). The absence of the KtrA potassium uptake pump extends the pulse duration, presumably by delaying the recovery of intracellular potassium stores. Notably, wild-type and Δ*ktrA* biofilms have a similar fraction of firing cells, despite their difference in average pulse durations. In contrast, Δ*trkA* and Δ*sinR* biofilms have similar pulse durations, even though Δ*trkA* biofilms contain the lowest and Δ*sinR* biofilms the highest fraction of firing cells (see Fig. S2.5 for single-cell traces from the model). Together, these strains show that the fraction of firing cells and average pulse durations can be separately modulated, allowing us to experimentally explore the phase space defined by the structure and dynamics of biofilms during signal transmission (Fig. 2.4F).

The different combinations of biofilm structure and dynamics that are accessible through genetic perturbations provide an opportunity to investigate why the wild-type cell-to-cell heterogeneity is organized near the critical percolation threshold. Motivated by the notion that biological processes carry not only a benefit, but also a cost, we asked whether the observed spatial organization of wild-type biofilms could be explained by the balance between the benefit and cost of signal transmission. The benefit is defined by the ability to successfully transmit the signal within the biofilm, since such signaling has been previously shown to increase the population-level fitness against chemical attack [1]. Therefore, we can experimentally define the population-level benefit of signaling based on the fidelity of signal transmission. Specifically, we measure the relative fraction of cells that relay the signal at the two most distant locations within the field of view of our experimental set up (approximately 25 cell lengths in Fig. 2.5B). We find that the wild-type and mutant biofilms that contain a fraction of firing cells that are near or above the critical percolation threshold can successfully transmit the signal without a decay in its amplitude (Figs. 2.5A,B). In contrast, the Δ*trkA* strain, which has a fraction of firing cells well below the percolation threshold (Figs 2.44D,F), fails to transmit the signal (Figs. 2.5A,B). We can now relate this experimentally determined benefit to the mathematical model

based on the fidelity of signal transmission. In particular, the model predicts that as a function of f, the benefit will sharply rise in a sigmoidal manner (Fig. 2.5C). This sudden rise in the population-level benefit is due to the sudden transition in connectivity at the percolation threshold that enables signal transmission through the system. Beyond the percolation threshold, the benefit is predicted to saturate, since a fully connected conduit for signaling has already been formed, and a further increase in the fraction of firing cells does not qualitatively alter signal transmission. Our experimental data are consistent with the mathematically predicted benefit function (Fig. 2.5C).

On the other hand, community-level benefit is also associated with a single-cell-level cost. Specifically, firing cells incur a metabolic burden during their electrical activity, as illustrated by the experimentally observed reduction in their cell elongation rate (Fig. 2.1B). Therefore, we define population-level cost as the fraction of firing cells multiplied by their mean signaling duration (Fig. 2.5D). The biofilm incurs greater cost with an increasing number of firing cells, or longer firing durations per cell. Consequently, the cost function increases gradually with the fraction of firing cells. While both the cost and benefit increase as a function of the fraction of firing cells, the smooth rise of the cost function and the sharp sigmoidal shape of the benefit function imply an intriguing cost-benefit relationship (Figs. 2.5C,D).

We find that the intersection of a nonlinear benefit function and a linear cost function gives rise to a non-monotonic benefit-to-cost relationship. Specifically, the cost rises at a constant rate, while the benefit jumps at the percolation threshold and then saturates (Figs. 2.6A,B). This suggests that the benefit-tocost ratio would be highest near the percolation threshold. Indeed, when we plot the benefit-to-cost ratio from the model as a function of the fraction of firing cells, we find a well-defined peak near the percolation threshold (Figs. 2.6C,D). The result does not depend on the specific way in which benefit and cost are compared: subtracting the cost from the benefit, for instance, also yields a peak near the percolation threshold (Fig. S2.6). The experimentally determined values place the wild-type biofilm near this region defined by the peak,

while the mutant biofilms are located away from this region (Fig. 2.6D). These results indicate that the spatial organization of heterogeneity in the wild-type biofilm promotes efficient signal transmission by residing near the percolation threshold.

We note that given a sharp rise in the benefit due to the critical phase transition, the benefit will outweigh the cost near the percolation threshold for a broad range of slopes of the cost function (Figs. 2.6C,D inset). We also note that linearity is not required, for as long as the cost function increases gradually, the benefit-to-cost function will always be dominated by the jump in the benefit.

2.4 Discussion

It has been suggested that biological systems across different scales exhibit properties consistent with critical phase transitions. This claim is often justified by the observation of scalefree behaviors, such as power-law dependencies [23, 24, 25]. However, two common concerns are that many biological systems lack an underlying theoretical justification of a critical phase transition, and that the biological purpose of operating near a phase transition is unclear [26]. Here we demonstrate that the spatial organization of a bacterial biofilm is consistent with percolation theory, which is well-known to exhibit a critical phase transition. Specifically, we observe a power law that arises at the predicted value (percolation threshold) and with the predicted exponent. Furthermore, we offer a biological rationale for why the system would be at criticality, by showing that the benefit outweighs the cost near the critical point. The scale-free nature of the critical point also suggests that efficient signal transmission is independent of the size of the biofilm. In other words, signals can be efficiently transmitted as the biofilm grows, without the biofilm having to adjust the fraction of firing cells. It is thus intriguing to speculate that a cost-benefit negotiation may be an organizing principle that drives the biofilm structure to the critical percolation threshold. Our findings suggest that the cost and benefit of signal transmission may play a role in promoting spatial heterogeneity that is organized near criticality. Consequently, the theory developed in statistical physics to describe criticality may also describe the spatiotemporal organization of diverse biological systems and provide a conceptual framework to uncover the functional pressures that drive these systems to phase transition points.

2.5 Methods

2.5.1 *Bacillus subtilis* Strains

We conducted all experiments with *B. subtilis* NCIB 3610. All strains used in this study can be found in Supplementary Table S2.1. Wild-type 3610 was a gift from W. Winkler (University of Maryland) [27]. All other strains were derived from it and verified by sequencing.

2.5.2 Biofilm Growth Conditions

We grew biofilms in MSgg medium containing 5 mM potassium phosphate buffer (pH 7.0), 100 mM MOPS buffer (pH 7.0, adjusted using NaOH), 2 mM MgCl2, 700 mM CaCl2,50mM MnCl2, 100 mM FeCl3,1mM ZnCl2,2mM thiamine HCl, 2 mM sodium citrate, 0.5% (v/v) glycerol and 0.4% (w/v) monosodium glutamate. Media were made from stock solutions immediately before experiments, and the stock solution of glutamate made fresh every two days.

2.5.3 Microfluidics and Experimental Conditions

24 hr before experiments, we streaked strains from -80 C glycerol stocks onto LB agar plates and grew overnight at 37 C. The day of experiments, we inoculated single colonies from LB plates into 5 mL of liquid LB media and grew in a 37 C shaker for $\sim$2.5-3 hr. We centrifuged LB-grown cultures at 4800 rpm for 2 min and resuspended cell pellets in MSgg medium. We then immediately loaded cells into a Y04D microfluidic plate using the CellASIC ONIX microfluidic system (EMD Millipore) [1]. After loading, we grew cells in the microfluidics at 37 C and 0.5 psi ($\sim$8 mm/s) flow for $\sim$2 hrs before changing temperature to 30 C and growing overnight under 1.5 psi flow ($\sim$24 mm/s). After 12 hr of growth in plain MSgg, ThT dye was flowed in at a concentration of 10 mM. Experiments were conducted under these conditions.

2.5.4 Percolation Theory

To describe the connectivity and clustering statistics of firing cells in the biofilm, we simulate cells on a regular two-dimensional lattice. Because cells in the experimental biofilms have a modal value of six neighbors (Fig. 2.1D), we use a triangular lattice, in which cells have six nearest neighbors to which they connect forming triangles [18]. Other lattices that would be good approximations of the biofilm predict similar results to those of the triangular lattice (Fig. S2.1). Percolation theory describes the statistics of lattices in which a fraction ϕ of cells are firing. Firing cells are positioned uniform randomly within the lattice.

Percolation theory predicts that for sufficiently large lattices there is a critical threshold ϕ_c at which several key features occur (Stauffer and Aharony, 1994). First, the probability of a connected path (a contiguous path of firing cells that spans from one side of the lattice to the other) transitions from 0 to 1 at ϕ_c (Fig. 2.1G). Second, at ϕ_c the distribution of cluster sizes becomes a power law, $p(n) \propto n^{-\alpha}$ (Fig. 2.1H), where a cluster is defined as a group of contiguous firing cells, and n is the number of cells in the cluster. For two-dimensional infinite lattices, the exponent is $\alpha = 187/91 \approx 2.05$ [18]. Below ϕ_c the distribution falls off exponentially (Fig. S2.2), and above ϕ_c the distribution acquires weight near the lattice size due to the emergence of a giant cluster (Fig. S2.2).

In all simulations we use a lattice size that corresponds to the approximate observation window in the experiments, $L = 35$ cell heights by $W = 200$ cell widths. Connectivity is determined along the shorter direction L, since this is the direction of signal propagation in the biofilm. The asymmetric geometry ($L \neq W$) is responsible for the deviation of the percolation threshold ($\phi_c = 0.45$) seen in the main figures from the predicted value for a symmetric triangular lattice ($\phi_c = 0.5$) [18]. Figs. 2.1G,H, and S2.2 were generated using 2000 realizations of the lattice.

2.5.5 Dynamical Model

To model the single-cell dynamics of electrical pulses in the biofilm, we utilized the FitzHugh-Nagumo (FN) model (Fig. 2.3A) [21]. The FN model is a minimal model of excitable dynamics and is commonly utilized for studying action potential dynamics in neurons. Here we use it to model the bucket-brigade mechanism of effective electrical activation of neighboring cells reported previously [2]. Specifically, we use a discretized Laplacian term to account for the cell-cell communication (Figs. 2.3A,C). In general, the parameters of this phenomenological model do not have a precise mechanistic interpretation, but rather are calibrated from the experiments as described below.

In all dynamical simulations, cells in the first row are initialized with $u = 1$ to trigger the excitable wave; all other cells are initialized with $u = 0$. We use a lattice of $L' = 100$ rows by $W = 200$ and record from a window of L =35 by $W = 200$ that is positioned just after the first row. Choosing $L' > L$ avoids boundary effects at the last row. We use an absorbing boundary at the last row and reflecting boundaries on the other three sides. To evolve the dynamics, we discretize the FN model in time using the fourth-order Runge-Kutta method with time step $\Delta t = 0.02$. For the cell-cell coupling we use $g_j = 1/2$ and 1/4 (Fig. 2.3A) for the two short-edge and four long-edge neighbors, respectively, corresponding to a rectangular cell with a 2-to-1 aspect ratio on a triangular lattice.

A fraction ϕ of cells are firing and are positioned randomly in accordance with percolation theory as described above. All firing cells have the same FN parameters, given below. Non-firing cells have the same parameters as firing cells, except that we reduce the recovery time τ by a factor of 60, which we find strongly reduces the firing propensity of these cells (Figs. 2.3D,E).

2.5.6 Model Calibration

We calibrate the parameters of the model (Fig. 2.3A) from the wild type (WT) data in the following way. The fraction of firing cells $\phi = 0.43$ is obtained directly from the experiments (Fig. 2.4D). The excitation strength ε must be larger than 1 because otherwise diffusion outpaces excitation and the wave does not propagate; therefore we set $\varepsilon = 10$ (note that because the model is phenomenological, the diffusion we describe here is effective and does not correspond to the diffusion of, say, the potassium ions between cells). The threshold u_0 must be significantly less than 1 because otherwise signal from a neighboring cell is insufficient to trigger an excitation and the wave does not propagate; we find that $u_0 = 0.02$ suffices (Fig. 2.3D). The recovery time of firing cells $\tau = 300$ is set such that the mean wavelength over 10 simulations is equal to the approximate experimental wavelength of 35 cells. Finally, we convert from dimensionless time τ to minutes by equating the mean pulse duration in the simulations to the experimental value (Fig. 2.4E). Pulse duration is averaged over all firing cells and defined as the time over which u ¿ 0.6. See Fig. S2.5 for single-cell time traces from model biofilms with parameters corresponding to each experimental strain.

2.5.7 Model Validation

We validate the model using one of the mutant strains, Δ*sinR*. This strain has a higher fraction $\phi = 0.74$ of firing cells than WT. We anticipate that because structure and dynamics are connected in the integrated model, changing the fraction of firing cells will also change the mean pulse duration. We test this expectation in the model, setting $\phi = 0.74$ and keeping all other parameters the same as WT. We observe in the simulations that the mean pulse duration rises from 18.1 min (WT) to 33.2 min (Δ*sinR*). In the experiments, we measure the mean pulse duration for Δ*sinR* to be 34.1 min, which agrees very closely with the value from the simulations. This validates the model and demonstrates that structure and dynamics are tightly connected in

the integrated model.

2.5.8 Cost-Benefit Curves

To determine the cost and benefit curves in Figs.2.5 and 2.6, we use the following procedure. In Fig. 2.5C, we vary ϕ while keeping all other parameters as calibrated above. For each ϕ value, we calculate the benefit as the average over 100 simulations of the ratio of the number of firing cells in the final five rows to that in the initial five rows. In Fig. 2.6D, we calculate the cost as the average over 100 simulations of the product of the fraction of firing cells and the mean pulse duration. In Figs. 2.6A–C, for each ϕ value, we vary τ in the range 5 to 1000 and measure the mean duration and benefit-to-cost ratio over 30 simulations for each τ value. Then we use linear interpolation to find the benefit-to-cost ratio corresponding to a particular duration. This produces curves of benefit-to-cost ratio vs. ϕ at fixed duration. Finally, we smooth these curves using a Gaussian filter of width 0.01, producing the result in Fig. 2.6C.

2.5.9 Time-Lapse Microscopy

We recorded phase-contrast and fluorescence images of biofilms at regular time intervals (between 3 and 10 min across experiments). For most experiments, we recorded phase, ThT fluorescence (for electrical signaling), and YFP fluorescence (for other analysis, see below). We used an Olympus IX83 inverted epifluorescence microscope with autofocus and a 40X, 0.6 NA or 100X, 1.4 NA objective, depending on the experiment. For each image, we used the minimum fluorescence exposure time that yielded good signal. For ThT images, exposure time was 17 ms and for YFP, exposure time was 150 ms.

2.5.10 Image Analysis

In order to segment single cells in each field of view, we took both ThT and YFP images with a 40X, 0.6 NA objective at the peak of each signal pulse as determined by the highest average ThT intensity of each field of view during signaling. Each field of view contained roughly 8000 bacteria. Cells expressed YFP from the citZ promoter, which gave a strong constitutive signal in each cell. From YFP images, we created thresholded binary images, from which we could identify the position and outline of each cell. We then thresholded ThT images at a fluorescence intensity value directly between the two peak peaks of the bimodal ThT intensity distribution (Fig. 2.2B) to create a binary image with contiguous high ThT regions corresponding to clusters of firing cells (Fig. 2.2C). Cluster sizes were measured by superimposing the high ThT cluster outlines on the binarized YFP image and counting the number of cells with a majority of their area inside each high ThT contour. The fraction of firing cells, f, was computed by dividing the number of firing cells (high ThT) by the total number of cells in the field of view. All processing was performed with custom Fiji macros.

2.5.11 Dynamic Analysis

Pulse durations come from single-cell tracking measurements, where a cell was considered to be pulsing if its ThT level was above the threshold described above. Tracking was performed with the mTrackJ Fiji plugin by manually clicking on cells in each frame of a time lapse movie [28]. To measure single cell cost (Fig. 2.1B) we measured elongation rate and ThT signal of single cells during a signal pulse with custom software written in MATLAB.

2.6 Acknowledgements

Chapter 2, in full, is a reprint of the material as it appears in Larkin JW, Zhai X, Kikuchi K, Redford SE, Prindle A, Liu J, Greenfield S, Walczak AM, Garcia-Ojalvo J, Mugler A, Süel GM,"Signal percolation within a bacterial community", *Cell Systems*, 2018. The dissertation author was a co-author of this paper. We acknowledge Massimo Vergassola, Munehiro Asally, Steve Lockless, Tolga Çağatay, Lev Tsimring, Terry Hwa, Uri Alon, and Michael Elowitz for helpful discussions. We acknowledge Dong-yeon D. Lee for assistance during strain construction.

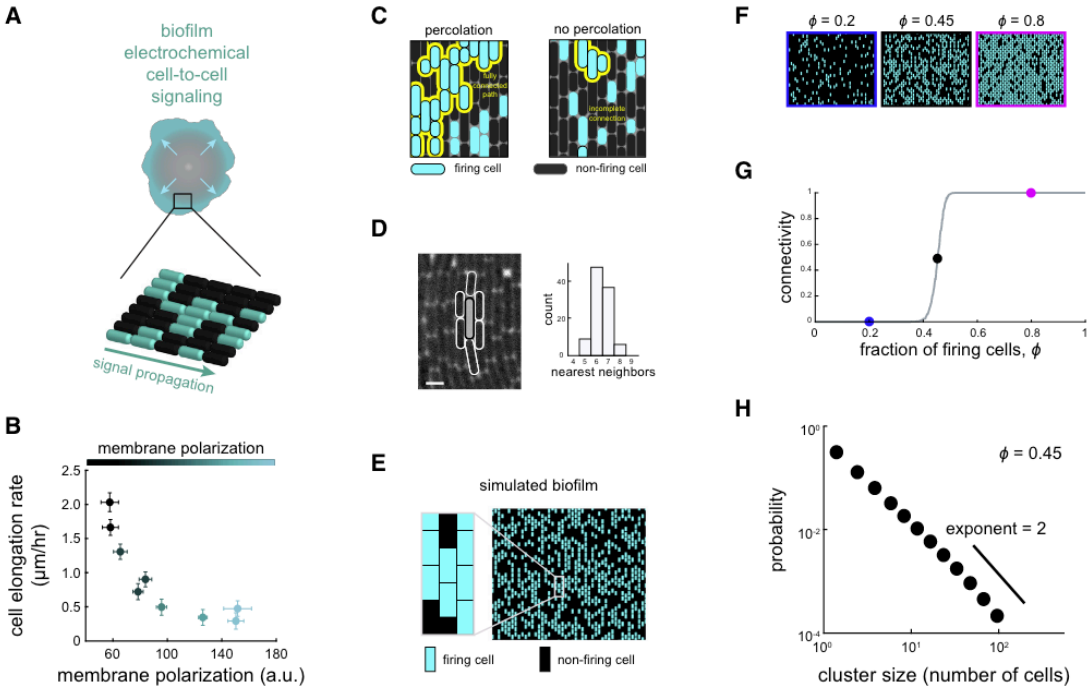

Figure 2.1: A Percolation Theory-Based Model for Electrochemical Signaling in Biofilms. **(A)** Biofilms undergo electrochemical signaling where the stressed biofilm interior periodically signals cells at the biofilm edge (arrows). Bottom cartoon depicts heterogeneous signaling where some cells participate in signaling (cyan), becoming hyperpolarized, while some cells do not participate (black). **(B)** Cell elongation rate is inversely correlated with membrane polarization, indicating a cost of electrical signaling activity to individual cells (N = 35 cells, error bars, ±SEM). **(C)** Percolation theory predicts the emergence of a connected path of firing cells (yellow outline) when the fraction of firing cells exceeds a critical value (left) but not below this critical value (right). **(D)** Image illustrating a method for counting the number of neighbors for a given cell, highlighted in white (left). Scale bar, 2 mm. Histogram (right) indicates the modal number of nearest neighbors is 6 (N = 100 cells). **(E)** Using the experimentally constrained nearest neighbor value of 6 (see also Fig. S2.1), firing and non-firing cells are randomly positioned on a two-dimensional lattice with probability ϕ (0.5 in this image). **(F)** Representative snapshots showing lattice simulations at various values of ϕ (see also Fig. S2.2). **(G)** Onset of connectivity (percolation) is predicted when ϕ exceeds 0.45. The ϕ values for the representative images in (F) are indicated on the graph by their respective colored circles. **(H)** Model-generated cluster size distribution at the percolation threshold (ϕ = 0.45), where clusters are distributed according to a power law.

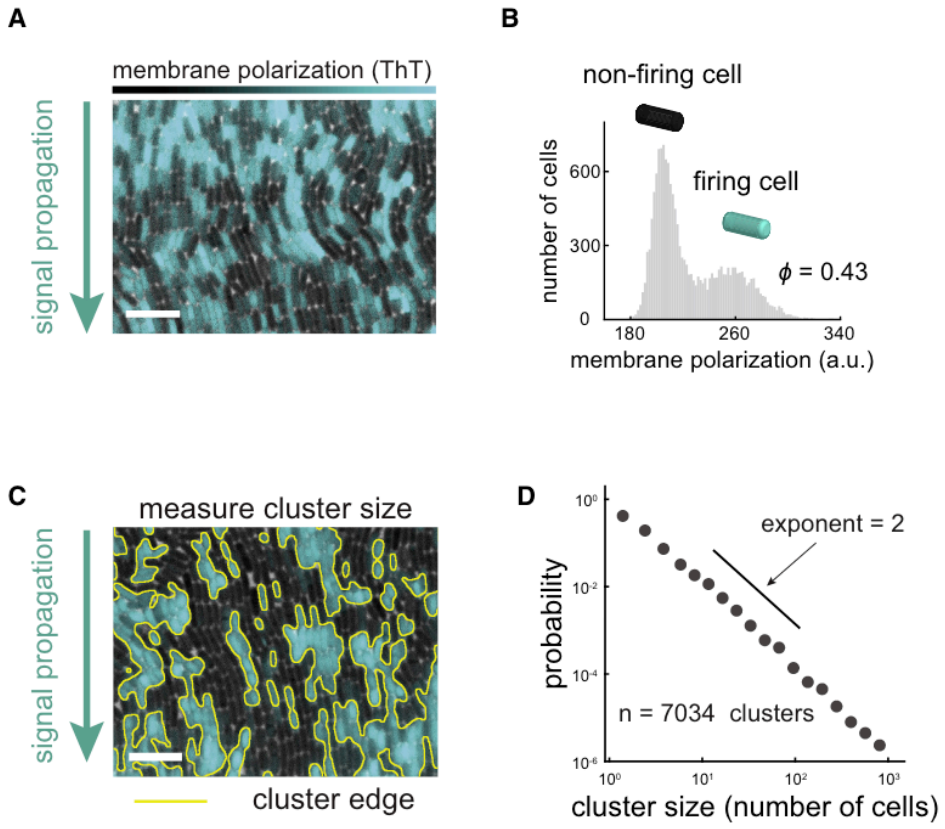

Figure 2.2: Electrochemical Signaling within Biofilms Is Heterogeneous at the Single-Cell Level.
(A) Membrane polarization is heterogeneous at the single-cell level within signaling biofilms. Cyan overlay indicates fluorescence of Thioflavin T (ThT), a cationic membrane polarization reporter. Scale bar, 10 mm (see also Fig. S2.3). **(B)** Histogram of individual cell ThT intensity (N = 14,936 cells) during a signal pulse. The bimodal shape of the histogram indicates that only a fraction of firing cells (cyan) participate in signaling (0.43 $\pm$ 0.02, mean $\pm$ SEM). **(C)** Firing cells are spatially clustered within biofilms. Yellow outlines indicate cluster edges identified by image analysis based on ThT fluorescence. Scale bar, 10 mm. **(D)** Cluster sizes (N = 7,034 clusters) are distributed according to a power-law decay across 3 decades with an approximate exponent of 2. These properties indicate that the arrangement of firing cell clusters within the biofilm can be described by percolation theory.

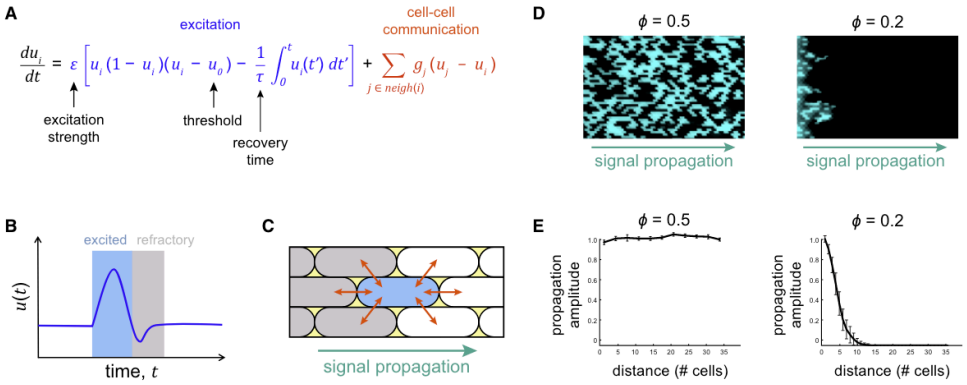

Figure 2.3: An Excitable Model for Signal Propagation in Biofilms.
(A) Model equation combines excitation (blue) and cell-cell communication (orange) to give rise to excitable propagation. The geometric factor gj is one-fourth at the cell poles and one-half otherwise. **(B)** A cartoon trace illustrates firing (blue-shading) followed by a refractory period (gray-shading) for a given excitable cell. **(C)** Cell-cell communication (arrows) allows directional signal propagation from one cell to another. Refractory cells are gray and excited cells are blue. **(D)** Example model snapshots depict complete signal propagation (direction indicated by arrow) in the regime above the percolation threshold (left, $\phi = 0.5$) and incomplete signal propagation below the percolation threshold (right, $\phi = 0.2$). Both cases have the same values for the dynamic parameters, $\varepsilon = 10$, $u_0 = 0.01$, $\tau = 300$ for firing cells or $\tau = 5$ for non-firing cells. **(E)** Example amplitude profiles for the images shown in (D) (error bars indicate $\pm$ SEM, N = 3).

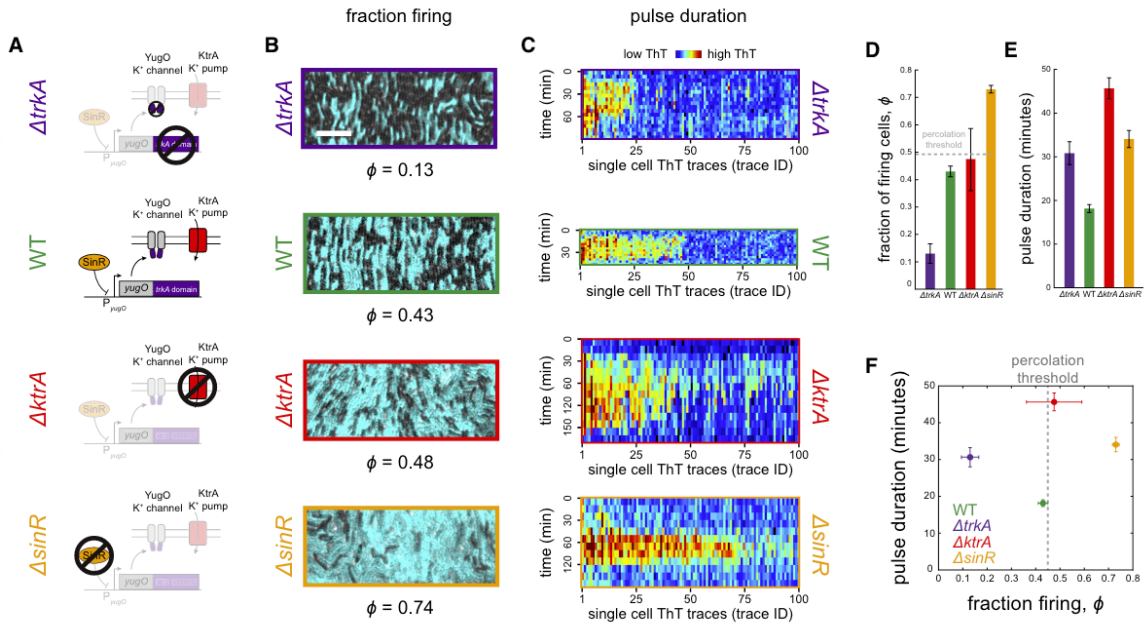

Figure 2.4: Experimental Tuning of Firing Cell Fraction and Pulse Duration with Mutant Biofilms.

(A) A series of cartoons illustrates the function of genes deleted in the mutant strains. **(B)** Representative images from time points of peak signaling activity depicting the fraction of firing cells for each strain (cyan ThT fluorescence). Scale bar, 10 mm. **(C)** Heatmaps depict single-cell ThT trajectories (N = 100) for all strains. Each column is one cell trace, with time progressing downward. The color scale varies across strains due to baseline fluorescence differences among experiments (see also Fig. S2.5). **(D)** Mutant strains exhibit decreased (Δ*trkA*, 0.13 ± 0.04, n = 7, mean ± SEM) or increased (Δ*sinR*, 0.74 ± 0.04, n = 4 and Δ*ktrA* 0.48 ± 0.11, n = 4) fraction of firing cells relative to wild-type (0.43 ± 0.02, n = 12). Wild-type is near, but slightly below, the percolation threshold, $\phi_c = 0.45$. The Δ*trkA* strain (purple), which lacks the gating domain of the potassium channel YugO, is expected to exhibit reduced signaling activity. The Δ*sinR* mutant (orange) lacks a transcription factor (SinR) that represses expression of YugO, resulting in higher signaling activity. **(E)** Pulse duration measurements, where pulse duration is defined as the amount of time membrane polarization remains above baseline level. All mutant strains (Δ*trkA* 30.6 ± 2.6, 124 cells, three biofilms, and Δ*ktrA* 45.7 ± 2.4, 204 cells, three biofilms, and Δ*sinR* 34.1 ± 2.0, 165 cells, three biofilms, mean ± SEM) have larger pulse durations than wild-type (18.1 ± 1.0, 383 cells, three biofilms). **(F)** A phase plot of pulse duration and fraction firing for each strain. Δ*trkA* lies below the percolation threshold (dotted line) and Δ*sinR* above, both with longer pulse duration than wild-type. Wild-type and Δ*ktrA* lie near the threshold, but with different pulse times (error bars, ± SEM).

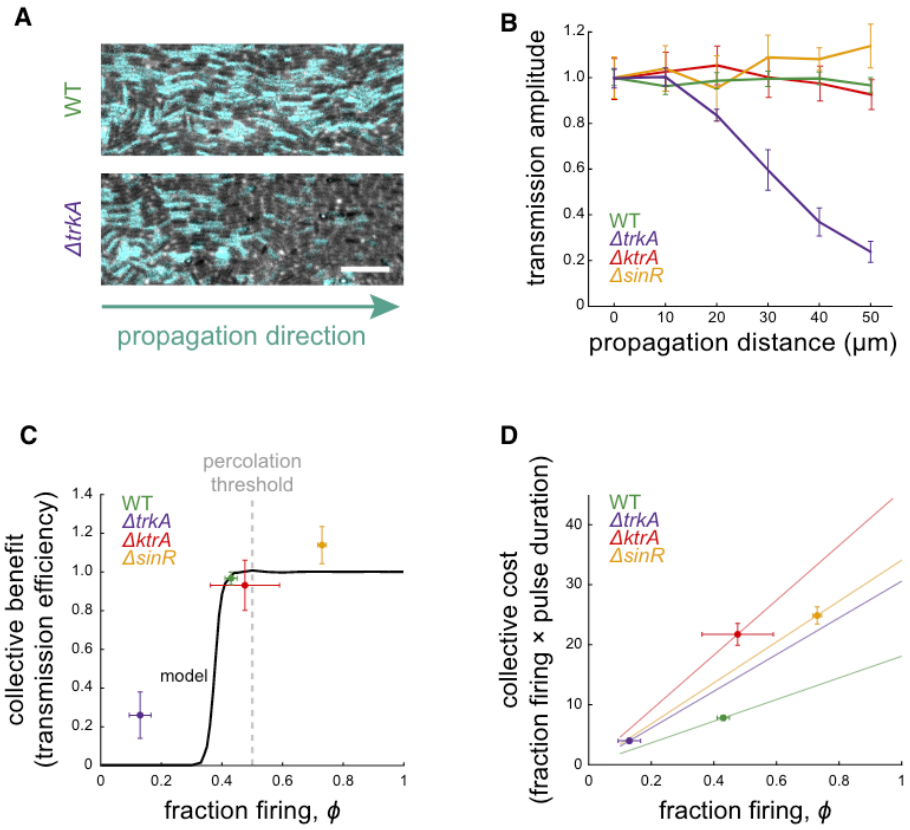

Figure 2.5: Signal Transmission Occurs near or above the Percolation Threshold.
(A) Phase images with overlaid ThT intensity (cyan) during peak signaling show steady signal propagation in wild-type (top) and spatial signal decay in Δ*trkA* (bottom). Scale bar, 10 mm. **(B)** Transmission amplitude measurements show that wild-type (n = 7), Δ*ktrA* (n = 4), and Δ*sinR* (n = 4) propagate the signal at a constant amplitude, while Δ*trkA* (n = 5) does not. Transmission amplitude is defined as the fraction of firing cells at a given position divided by the firing fraction at the beginning of the field of view (error bars, ± SEM). **(C)** Collective benefit of signaling is defined as the ratio of transmission amplitudes at the biofilm edge and at the beginning of the field of view. Experimental data are shown by points (error bars, ± SEM). The model output for wild-type parameters (black curve) illustrates the nonlinear nature of collective benefit. **(D)** Collective cost of signaling is defined as the product of the firing cell fraction, f,andmean pulse time. Experimental data are shown as points (error bars, ± SEM). Lines represent the cost that would be incurred for each strain given its mean pulse time.

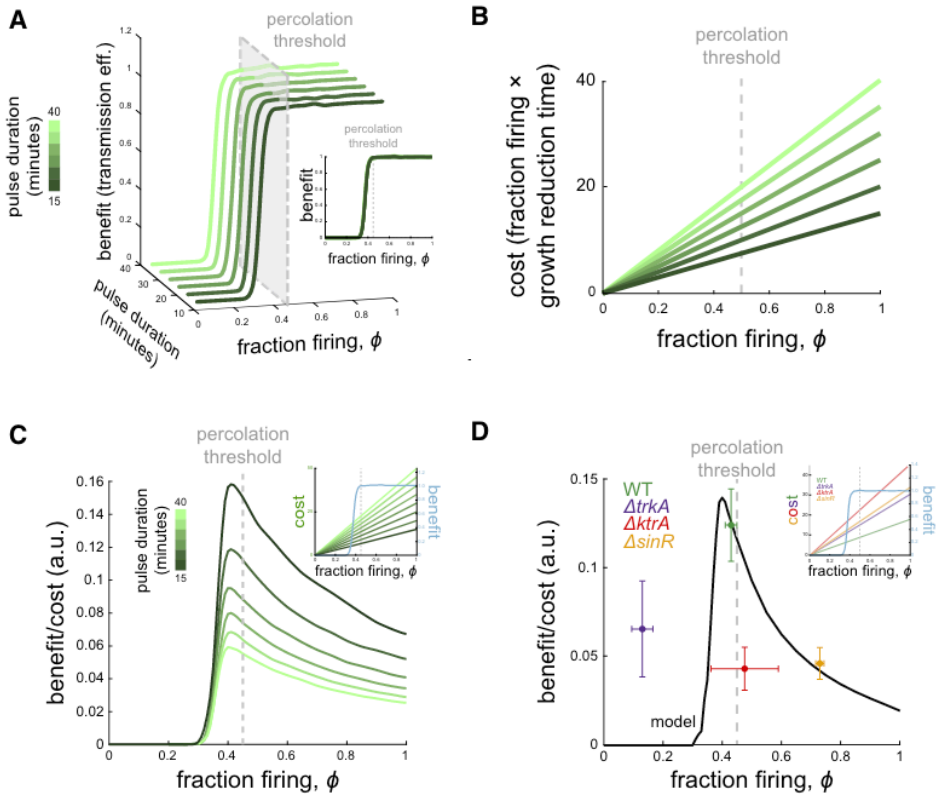

Figure 2.6: Cost-Benefit Negotiation in Signal Transmission.
(A) The benefit (transmission efficiency) is plotted for different dynamic parameters as a function of ϕ and resulting pulse time (green color scale). When plotted as a function of ϕ only, the curves line up with benefit rising near the threshold (inset). **(B)** The cost function is plotted for the corresponding benefit curves from (A). **(C)** Benefit/cost ratio is plotted as a function of ϕ for the different model curves in (A) and (B), illustrating that, no matter the dynamic model parameters, benefit/cost ratio has a peak near the percolation threshold. This comes from the fact that benefit is highly nonlinear in f, while cost increases smoothly for any set of dynamic parameters (inset). **(D)** Measured benefit/cost ratio is plotted for each strain (dots, error bars indicate ± SEM), along with the model output given wild-type parameters (curve). The ratio exhibits a peak due to the linear cost but highly nonlinear benefit, with wild-type near the maximum (see also Fig. S2.6). Inset plot overlays cost and benefit on separate y axes.

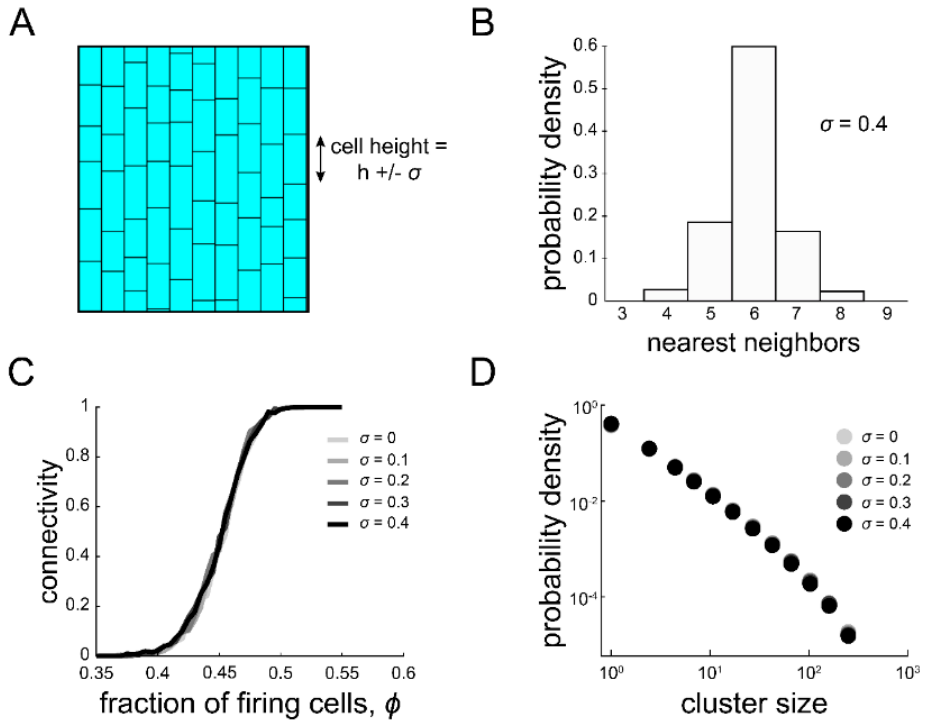

Figure S2.1: Disordered lattices have the same percolation properties as triangular lattices. **(A)** A disordered lattice may be created by starting with a triangular lattice and adding random noise (σ) to the height of each cell. **(B)** his yields a model biofilm with a distribution of nearest neighbor numbers, as shown in this histogram from a $\sigma = 0.4$ biofilm. Some cells have more than 6 nearest neighbors, some fewer. **(C)** These perturbations do not affect the percolation threshold, as shown in this connectivity plot near the threshold value of $\phi_c = 0.45$. $\sigma = 0$ represents the triangular lattice used in the paper. All curves overlap. **(D)** For different σ values, the cluster size distribution is not significantly changed near the percolation threshold, as shown in this cluster size distribution plot for different σ values.

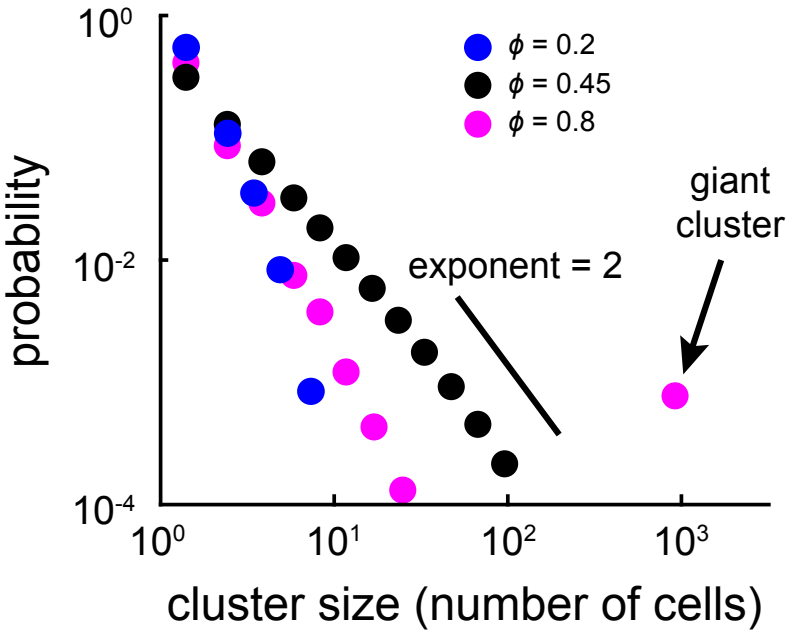

Figure S2.2: Cluster size distribution in model biofilms changes with fraction of firing cells. Model-generated cluster size distributions for values of ϕ depicted in Fig. 2.1F, G. Only when $\phi = \phi_c$, are clusters distributed according to a power-law (black circles). Above the percolation threshold (magenta circles), a giant cluster develops near the system size.

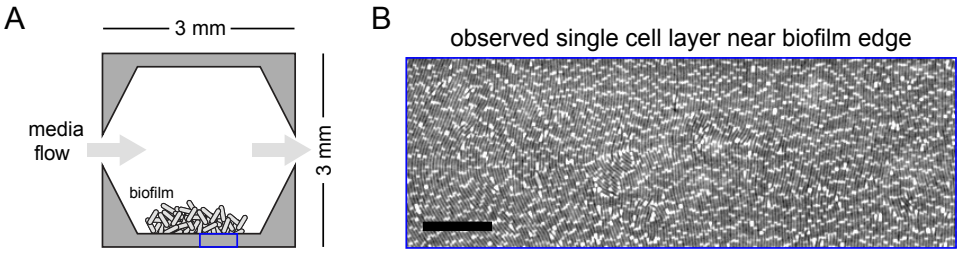

Figure S2.3: Microfluidic system for single molecule measurements of biofilms.
(A) Schematic of microfluidic device used in these experiments. Cells are seeded under a strip of PDMS (bottom) and allowed to grow into a biofilm as media flow is controlled. During biofilm growth, the edge region under the PDMS strip is confined to single cell thickness (e.g. blue rectangle), enabling imaging at single-cell resolution, as shown in the phase image in **(B)**, Scale bar, 20 μm.

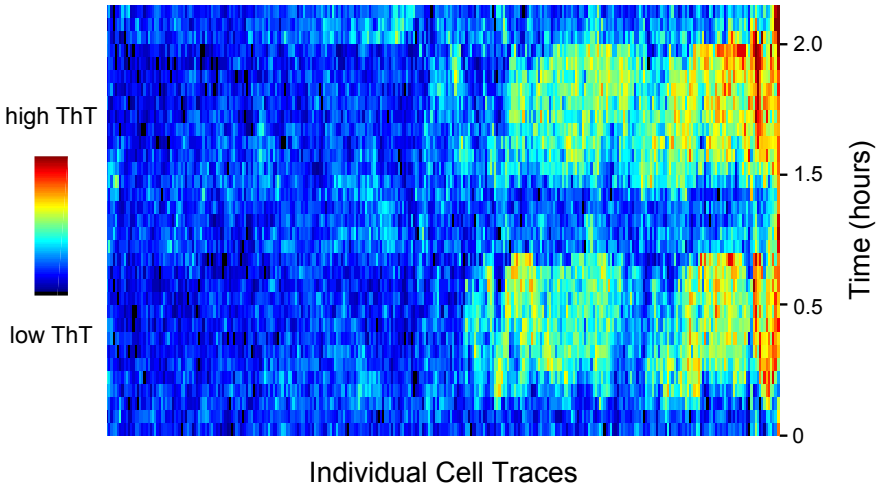

Figure S2.4: Cells generally do not switch signaling state between pulses.
A heatmap of 320 single cell ThT traces from two consecutive pulses in a wild-type biofilm. Each column is a ThT trace from one cell with time increasing along the vertical axis. The traces are organized with hierarchical clustering. The heatmap illustrates that the cells maintain their firing state. Cells that fire on the first pulse have a much higher probability of firing on the second pulse than those that do not and vice versa.

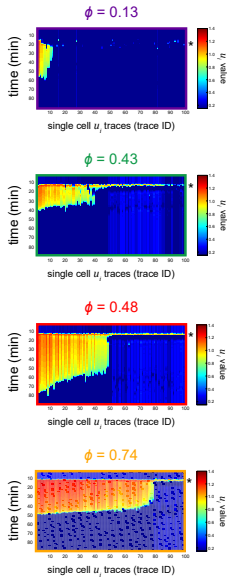

Figure S2.5: The model predicts heterogeneous single-cell time traces.
Heatmaps displaying time traces from the model for 100 randomly chosen cells from biofilms with parameters matched to those of the four experimental strains (see Methods for details). For each heatmap, a single column is that trace from one cell and time moves from top to bottom. The time point of excitation for each heatmap is marked with an asterisk. Compare to the experimental heatmaps from Fig. 2.4C of the main text.

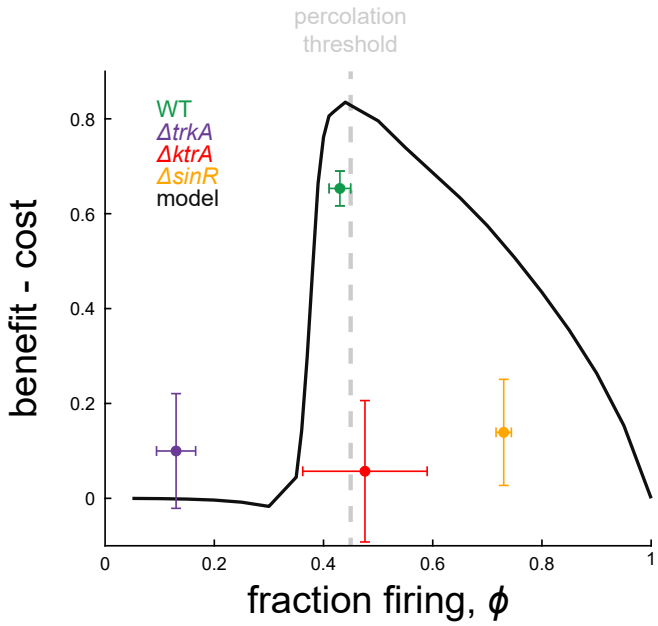

Figure S2.6: Benefit minus cost yields a peak near the percolation threshold.
Benefit minus cost is plotted as a function of fraction of firing cells for experimental data (colored points) and the model with wild-type parameter values (black line). Because benefit is a number between 0 and 1 and cost unbounded, we normalize cost by dividing it by the highest pulse time value measured. The curve bends down at higher ϕ values because the pulse time from the model slightly increases with ϕ for the same τ value (see Methods). As with benefit divided by cost, this function exhibits a peak near the percolation threshold.

Table S2.1: *Bacillus subtilis* strains used in Chapter 2.

Strain	Genotype	Source
Wild type	*B. subtilis* NCIB 3610	[27]
P_{citZ}-YFP	*sacA*::P_{citZ}-*yfp* (Cm^R)	This study
Δ*trkA*	*trkA*::Neo^R	[2]
Δ*sinR*	*sinR*::Neo^R	[29]
Δ*ktrA*	*ktrA*::Erm^R	[30]

Chapter 3

Electrochemical potential enables dormant spores to integrate environmental signals

3.1 Abstract

The dormant state of bacterial spores is generally thought to be devoid of biological activity. We show that despite continued dormancy, spores can integrate environmental signals over time through a pre-existing electrochemical potential. Specifically, we studied thousands of individual *Bacillus subtilis* spores that remain dormant when exposed to transient nutrient pulses. Guided by a mathematical model of bacterial electrophysiology, we modulated the decision to exit dormancy by genetically and chemically targeting potassium ion flux. We confirmed that short nutrient pulses result in step-like changes in the electrochemical potential of persistent spores. During dormancy, spores thus gradually release their stored electrochemical potential to integrate extracellular information over time. These findings reveal a decision-making mechanism that operates in physiologically inactive cells.

3.2 Introduction

The formation of bacterial spores (sporulation) is a common and well-characterized survival strategy in many microbial species [31, 32, 33]. Spores are partially dehydrated cells enclosed by a protective coat that can survive environmental extremes and remain dormant for years, which need to be robust to environmental fluctuations to avoid exiting their dormant state (germinating) prematurely. At the same time, spores need to germinate if they detect favorable conditions [34] (Fig. 3.1A). Germination requires the re-hydration of the spore which is promoted by the release of Calcium-Dipicolinic Acid (CaDPA) [35]. Aside from degradation of RNA immediately following sporulation [36], dormant spores appear to be deprived of measurable metabolic or biological activity [37]. Therefore, it remains unclear whether dormant spores possess any activity that could affect the choice of whether or not to germinate. We thus tested whether dormant *Bacillus subtilis* spores experience any physiological changes in response to subtle environmental signals that do not trigger germination. Addressing these questions could reveal how spores reconcile their robust dormant state with the need to process extracellular information and make an informed decision on whether to continue or exit their dormancy.

Spores can be pre-treated with nutrients to promote germination [38, 39, 40]. TThese findings imply that spores can somehow integrate extracellular signals despite their dormancy, and thereby alter their future likelihood of triggering germination. While there are no well-established mechanisms for dormant cells to integrate extracellular information, the ability of spores to modulate their future response suggests a conceptual similarity to a decision-making mechanism in neuroscience known as integrate-and-fire [41, 21]. TThis mechanism describes how neurons respond to small synaptic inputs before reaching the threshold that triggers an action potential [42]. It is unclear whether dormant spores employ a similar mechanism to process environmental inputs and modulate their approach towards a threshold that triggers germination.

Given the physiological inactivity of spores, we investigated a possible integration mech-

anism based on passive ion flux, which does not require cellular energy. Our findings indicate that physiologically inactive spores integrate environmental signals by modifying pre-existing ion gradients that were established during sporulation. Dormant spores can thus use stored electrochemical potential energy to regulate their cell-fate decision without requiring de-novo ATP synthesis. In this way, spores can alter their distance to the germination threshold depending on environmental inputs, while still in the dormant state. This mechanism also reconciles the robust dormancy of spores with the ability to gradually become sensitized to future environmental signals.

3.3 Results

3.3.1 *Bacillus subtilis* spores can remain dormant despite exposure to germinant pulses

We confirmed that similar to laboratory strains, undomesticated Bacillus subtilis spores can be pre-treated with short nutrient (germinant) pulses to increase the likelihood of germination. Specifically, we imaged spores (Fig. 3.1B) within a microfluidic device that allows single-cell monitoring and precise control over media conditions (see Methods). We optically tracked the switch in phase-contrast brightness that results from the re-hydration of spores during germination [34, 43] (Fig. 3.1C, Fig. S3.1A,B). Using this experimental approach, we exposed thousands of spores to a single short germinant pulse (10 mM L-alanine for 3 minutes), and found that 95% of spores remained dormant (95.2% $\pm$ 1.9%, n = 2,244; Fig. 3.1D). We used the germinant L-alanine because it is a naturally occurring nutrient that triggers germination through designated receptors in bacterial spores [44]. Spores that did not germinate upon stimulation remained dormant for at least the next 20 hours of imaging (Fig. S3.1C). Any spore that did germinate in response to the germinant pulse did so on average within 15 minutes (14.85 $\pm$ 1.07, n = 1,831; Fig. S3.1D).

To quantify the integration capacity of spores, we applied a second germinant pulse, separated by 2 hours from the first pulse to ensure that germination in response to the first pulse of germinant had subsided. After the second pulse, approximately half of the remaining spores germinated (52.1% $\pm$ 6.2%). TThe germination propensity of spores was independent of their location within the microfluidic chamber (Fig. S3.2). We defined the spore's integration capacity as the population-level change (difference) in the germination probability in response to two consecutive germinant pulses (Fig. 3.1E).The germination probability increased by 47% $\pm$1% (mean $\pm$ SD, n=9 replicate populations) between the first and second pulse. Spores thus become sensitized by the first exposure and appear to move closer towards a germination threshold.

3.3.2 A mathematical model of the role of ion flux in responding to germinant pulses

To explain how physiologically inactive spores could integrate information about germinant exposure over time, we explored an ion flux as a mechanism, since this process could occur passively with pre-existing ionic gradients established during sporulation. Other processes such as de-novo gene expression and enzymatic activity typically require energy, which is highly limited in spores. In particular, we focused here on the flux of potassium, since it is the most abundant intracellular ion in bacteria, and has physiological roles in the stress response of *B. subtilis* [2, 45, 46, 30]. Furthermore, potassium ions have been proposed to stabilize the formation of bacterial spores [47]. To investigate the possible role of potassium ion flux in dormant spores, we developed a mathematical model based on the Hodgkin-Huxley (HH) framework [48] (Fig. 3.1F, Appendix B). Our model describes how potassium ion flux can drive a spore towards a fixed germination threshold via an integrate-and-fire mechanism, without requiring any physiological activity.

Our mathematical model assumes that potassium ions enter or leave a spore via passive transport through both selective potassium channels and non-specific ion channels. The direction and rate of potassium flux across the spore membrane depend on the potassium ion concentration gradient, as well as on the membrane potential of the spore [2, 45, 46, 30] (see Appendix B). We assume that spores contain high amounts of potassium [49, 50], which would result in ion efflux when channels are open. We also assume that ion pumps are inactive during dormancy, given that they require ATP for transport, which is highly limited and not actively produced in spores [36]. Furthermore, the model assumes that ion channels (both potassium specific and non-specific) are closed until germinant is added. The channels open in the presence of germinant and close in its absence. Finally, we assume that the initial potassium content of spores has some variability, and that germination begins when a spore's internal potassium concentration drops below a certain

value ((that is, it reaches the germination threshold,, Fig. 3.1G,H). Given these assumptions, the model predicts that, when exposed to consecutive short germinant pulses, few spores germinate during the first pulse, whereas most spores do so during the second, or subsequent pulses (Fig. 3.1I). This increase in the germination probability of spores is consistent with our experimental observations (Fig. 3.1D). Different germinant concentrations in the first pulse did not markedly change the fraction of germinated spores (Fig. S3.3). In contrast, the germinated fraction increased with higher concentration of L-alanine in the second pulse. This difference in the sensitivity of spores to the first and second germinant pulse concentrations further demonstrates integration of information. Efflux of potassium from dormant spores was also confirmed with an extracellular potassium indicator, Asante Potassium Green-4 tetramethylammonium salt (APG-4 TMA) (Fig. S3.4A,B). Our modeling approach thus shows how spores might use intracellular potassium concentration to integrate information about previous germinant exposures and change their sensitivity to future exposures.

3.3.3 Initial potassium concentrations define the distance to the germination threshold

Our mathematical model assumes that the initial potassium content defines the distance to the germination threshold (Fig. 3.1G,H). TTo test this, we generated a mutant strain in which the KtrC subunit of the KtrCD potassium importer was deleted, which is expected to lower intracellular potassium content and, consequently put the spore closer to the threshold compared to wild-type spores (Fig. 3.2A). KtrC is the major potassium importer expressed in the inner spore membrane during the sporulation process [51], enabling potassium uptake [52, 53] (Fig. 3.2B,C). By generating spores in the presence of an intracellular potassium indicator, Asante Potassium Green-4 Acetoxymethyl ester (APG-4 AM), we confirmed that the Δ*ktrC* spores contain less potassium compared to wild-type spores (Fig. S3.4C-F). Accordingly, the Δ*ktrC* spores are mathematically predicted to be more likely to germinate in response to the first germinant pulse

(Fig. 3.2D). Indeed, measurements show that 42% of the Δ*ktrC* spores germinated after the first pulse, compared to 5% of the wild-type spores (Fig. 3.2E-G). The germinated fraction of Δ*ktrC* spores then further increased after the second pulse (Fig. 3.2H). We obtained similar results with spores lacking KtrD, the other subunit of the KtrCD potassium importer (Fig. S3.5A).

Given the high germination probability of Δ*ktrC* spores, almost the entire population (94%) germinated after only two germinant pulses (Fig. 3.2G). However, because the deletion of KtrC does not affect potassium efflux in spores, the integration capacity of Δ*ktrC* spores is comparable to that of wild-type spores (Fig. 3.2I). To further confirm that the lower potassium content of Δ*ktrC* spores caused the higher sensitivity to germinant pulses, we supplied additional potassium during sporulation of Δ*ktrC* cells. Increasing the potassium content in Δ*ktrC* spores should increase their distance to the germination threshold, which in turn would be reflected in a decrease in their germination probability (Fig. S3.5B). In agreement with those expectations, the addition of 150 mM of potassium in the sporulation medium resulted in Δ*ktrC* spores that responded to germinant pulses similarly to wild-type spores (Fig. S3.5C,D). These results are consistent with the modeling prediction and support the idea that the initial intracellular potassium concentrations of spores specifically define their distance to the germination threshold.

3.3.4 Potassium ion channels contribute to the integration capacity of spores

We investigated the modeling prediction that spores use potassium efflux to integrate over consecutive germinant pulses. To this end, we studied a mutant strain lacking the YugO potassium ion channel (29) (Fig. 3.3A,B). We confirmed that Δ*yugO* spores contain less potassium than do wild-type spores by using the intracellular potassium indicator APG-4 AM (Fig. S3.4C-F). Therefore, the Δ*yugO* spores should be initially closer to the germination threshold and be more sensitive than wild-type spores to the first germinant pulse (Fig. 3.3A,D). On the other hand, the absence of the YugO channel also implies a reduced potassium efflux in response to germinant

pulses. According to our model, such reduced potassium efflux in germinant-exposed spores will lower their integration capacity, and thus the germination probability for subsequent germinant pulses will be lower (Fig. 3.3D). In other words, the Δ*yugO* spores will not markedly increase their sensitivity to consecutive germinant pulses, which should distinguish this strain from the wild-type and the Δ*ktrC* strains. These mutant spores are therefore predicted to approach the germination threshold more gradually due to reduced potassium efflux.

We experimentally tested these predictions. Essentially, the progressions of the wild-type and the Δ*yugO* spores towards the germination threshold are predicted to exhibit a cross-over point (Fig. 3.3D). Experiments confirmed that the Δ*yugO* spores have a higher response than wild-type to the first germinant pulse (with 30% vs 5% of the spores germinating, respectively) (Fig. 3.3E,F,H). However, these spores lacked the increase in germination probability in response to subsequent pulses, exhibited by the wild-type spores (Fig. 3.3I). This in turn reflects a substantial loss in integration capacity of the Δ*yugO* spores when compared to wild-type (Fig. 3.3J, Fig. S3.6). The phenotype of the Δ*yugO* spores (high initial germination probability, and low integration capacity) is thus consistent with our modeling predictions. Importantly, the Δ*yugO* strain also indicates that reduced efflux of potassium decreases the integration capacity of spores. These results suggest that potassium efflux serves as an integration mechanism that modulates the approach to the germination threshold.

Given the complex phenotype of the Δ*yugO* strain, we turned to chemical perturbations of potassium flux in wild-type spores to independently determine whether potassium flux underlies the integration capacity of spores. We confirmed that modifying the external potassium concentration changed the integration capacity of wild-type spores (Fig. S3.6). Specifically, the absence of potassium in the media, expected to promote higher potassium efflux in spores, increases the integration capacity (from 0.47 ± 0.01 to 0.63 ± 0.02). In contrast, increasing extracellular potassium concentration lowers the integration capacity (RM + 600 mM KCl: 0.32 ± 0.01; RM + 1 M KCl: 0.03 ± 0.01). To discard the possibility that this reduction in integration capacity is

due to increased osmotic stress, we show that adding 1 M sorbitol has no effect on integration capacity (RM + 1 M sorbitol: 0.44 ± 0.02). The electrochemical gradient of potassium thus influences the integration capacity of spores.

We also tested how the integration capacity of wild-type spores is affected by blocking potassium channels with the drug quinine (1 mM; Fig. 3.3A,C, Figs. S3.4B, S3.6) [54, 55, 56, 57]. According to our model, such blocking of potassium channels is expected to specifically reduce the germination probability in response to consecutive germinant pulses (Fig. 3.3D). In agreement with this prediction, treatment of spores with quinine reduced the response of wild-type spores to the second germinant pulse, with around 80% of the spores remaining dormant, in comparison with around 45% in the absence of the drug (Fig. 3.3G,I). These results support the proposed integrate-and-fire mechanism by showing that similar to the deletion of the YugO channel, chemical blocking of potassium efflux in wild-type spores also impairs their integration capacity (Fig. 3.3J, Fig. S3.6).

3.3.5 Changes in the electrochemical potential of dormant spores

Our mathematical model proposes that the flux of potassium ions driving the processing of information during dormancy is modulated by the electrochemical potential of the spores. According to the integrate-and-fire mechanism, spores that are further from their germination threshold would require multiple germinant pulses to reach the threshold, each pulse causing an incremental electrochemical potential change (Fig. 3.4A). Specifically, the transient efflux of potassium cations triggered by germinant pulses is mathematically predicted to increase the negative electrochemical potential of spores in a step-like manner, even when the pulses do not trigger germination (Fig. 3.4B). To test this prediction, we used a previously characterized cationic fluorescent dye (Thioflavin-T, ThT) to measure changes in the electrochemical potential of dormant spores (see Methods) [2, 58]. As spores are notoriously impermeable to most chemicals [59], we expected that peripheral staining by ThT would reflect the spore's overall

negative electrochemical potential [47].

To experimentally test our modeling prediction of electrochemical potential jumps, we tracked thousands of individual wild-type spores over time and simultaneously imaged phase-contrast and ThT fluorescence intensities (Fig. 3.4C-F). Spores that did not trigger germination exhibited sudden changes in their electrochemical potential in response to germinant pulses. Spores that required multiple germinant pulses to trigger germination exhibited a multi-step progression before reaching their germination threshold. These increases in the ThT signal are not due to increased spore permeability, as ThT continued to stain the spore's periphery and did not transition to its interior (Fig. 3.4D). Therefore, accumulation of ThT on the spore periphery appears to reflect changes in the ionic content of the spore. We observed no characteristic changes of the phase-contrast brightness of dormant spores during the increases in the ThT signal (Fig. S3.7A). We also tested L-valine, another naturally occurring germinant [44], and observed similar changes in ThT signal (Fig. S3.7B). Furthermore, we used another positively charged dye, Tetramethylrhodamine methyl ester (TMRM), commonly used to measure the electrochemical potential of cells [60]. TMRM also stained the periphery of spores, and increases in the TMRM signal amplitude were qualitatively similar to those measured with ThT (Fig. S3.8A,B). To validate that the observed jumps in fluorescence during germinant additions were not simply a staining artifact, we synthesized a charge-neutral version of ThT (Fig. 3.4E inset, Figs. S3.8C,D, S3.9, Methods, and Appendix B). Although this charge-neutral ThT dye also stained the spore periphery, we observed no increases in the signal amplitude during germinant pulses. Instead, the fluorescence signal of the neutral ThT dye monotonically decayed over time likely due to photobleaching. To exclude the possibility that the observed changes in electrochemical potential could be related to the release of CaDPA during the initiation of germination, we generated a mutant strain lacking a subunit of the SpoVA channel, namely SpoVAF (Fig. S3.10A). This subunit is essential for effective CaDPA release during germination, and its deletion causes a delay in germination [61]. Deletion of SpoVAF slowed the response time of spores to L-alanine

(Fig. S3.10B). However, loss of Δ*spoVAF* did not impact the electrochemical potential changes we observed in spores (Fig. S3.10C,D), indicating that CaDPA release is not required for the integration of information in dormant spores. Together, these results demonstrate that germinant pulses cause sudden changes in the electrochemical potential of spores that otherwise remain dormant. As predicted, spores that required multiple germinant pulses to initiate germination also exhibited multiple jumps in their electrochemical potential, indicating their greater distance to the germination threshold. The ability to visualize and observe a multi-step and gradual approach of dormant spores towards their germination threshold provides further evidence in support of the integrate-and-fire mechanism.

We investigated whether the integration capacity that we determined from population-level statistics correlated with the independently observed jumps in the electrochemical potential of individual spores. In particular, a higher integration capacity should correlate with a higher change in electrochemical potential. We therefore measured germinant-induced changes in the electrochemical potential for thousands of spores obtained from various perturbations considered in this study (Fig. 3.4F,G). Higher integration capacity correlated with a higher average increase in electrochemical potential (Fig. 3.4H). Specifically, wild-type and Δ*ktrC* spores, which have similarly high changes in electrochemical potential, also exhibited relatively higher integration capacities. Furthermore, the Δ*yugO* and the quinine-exposed wild-type spores, which both exhibited lower average changes in their electrochemical potential, had reduced integration capacities. These findings support the prediction that dormant spores integrate environmental information through ion flux-induced changes in their electrochemical potential.

3.4 Discussion

We studied how physiologically inactive spores detect and respond to transient germinant pulses. Our results reveal that despite their dormancy, spores can integrate extracellular information and alter their intrinsic state. This ability to process information appears to be supported by pre-existing ionic gradients generated during sporulation. In this way, dormant spores can reach the decision to initiate germination by using electrochemical potential energy, rather than requiring a source of cellular energy, such as ATP. Spores may thus be analogous to a biological capacitor, in that they store and utilize an electrochemical potential to move closer to the germination threshold (Fig. 3.4I). The integrate-and-fire model proposed here provides both a conceptual and mechanistic explanation for how spores can respond to an environmental signal despite being physiologically inactive. The ability to sum inputs over time prior to reaching a threshold ensures that germination is triggered only when favorable conditions persist, while also ignoring small environmental fluctuations. While the integrate-and-fire model is used to describe how neurons process information, our work suggests that this concept may represent a more general solution to the need for information-processing in diverse biological systems including energy-limited cells.

3.5 Methods

3.5.1 Strains

All experiments were performed using the *Bacillus subtilis* strain NCIB 3610. The wild-type strain was a kind gift from W. Winkler [27] (University of Maryland). All strains used in this study can be found in Supplementary Table S3.1. The Δ*ktrC* and Δ*spoVAF* strains were made by PCR amplifying 1 kb regions upstream and downstream of the gene to be deleted and cloning them into the pER449 vector (gift from W. Winkler) flanking a spectinomycin resistance cassette. NEB turbo competent *E. coli* cells (New England Biolabs, Ipswich, MA, USA) were used for cloning purposes. Constructs were sequence verified and chromosomally integrated using a standard one-step transformation procedure [62]. Luria Broth (LB) agar plates containing appropriate antibiotics were used to select *B. subtilis* transformants (spectinomycin, 100 μg ml-1; neomycin 9 μg ml-1; tetracycline 6 μg ml-1)

3.5.2 Growth conditions

Sporulation was induced by resuspension medium (RM); composition per 1 L: 46 μg $FeCl_2$, 4.8 g $MgSO_4$, 12.6 mg $MnCl_2$, 535 mg NH_4Cl, 106 mg Na_2SO4, 68 mg KH_2PO4, 96.5 mg NH_4NO_3, 219 mg $CaCl_2$, 2 g monosodium L-glutamate [63]. For RM without potassium used in Fig. S3.4, KH_2PO_4 was replaced with an equivalent amount of NaH_2PO_4. Germination was induced by 10 mM L-alanine, a condition typically employed in *Bacillus subtilis* germination studies [64, 65], or 100 mM L-valine. Monosodium L-glutamate and L-alanine solutions were made fresh weekly.

3.5.3 Preparation of spores with the Resuspension Method

Spores were prepared according to the Resuspension Method, known to promote sporulation in *B. subtilis* strain NCIB 3610 [63]. A single *B. subtilis* colony was used to inoculate 5 mL of LB, and incubated overnight in a shaking incubator at 37 °C (200 rpm). The culture was diluted in 20% (v/v) LB at OD600 0.1 and incubated at 37 °C with shaking until reaching OD_600 0.6 - 0.8. The culture was then centrifuged at 4,000 rpm for 10 min, resuspended in 1 volume of pre-warmed RM, transferred to a large vessel (250 mL Erlenmeyer flask for 50 mL culture) to ensure aeration, and incubated for three days at 37 °C in a shaking incubator (200 rpm).

The resulting spore suspension was washed with distilled water three times and suspended in 1 volume of distilled water. The spore suspension was stored at 4 °C.

3.5.4 Preparation of spores containing APG-4 AM and measuring APG-4 AM fluorescence

Asante Potassium Green 4 AM (APG-4; ION Biosciences, Texas, USA), a cell-permeant potassium fluorescence indicator dye, was used to measure intracellular spore potassium concentration. Spores were prepared according to the method described above, with 2 μM APG-4 AM added to RM during the incubation time of three days. Spores were then washed and stored as described above. For fluorescence measurements, spores were placed in agar pads made from RM + 1.6% low-melting point agarose. Phase contrast and fluorescence snapshot images were taken with a Hamamatsu Orca-Flash4.0 LT+ camera under a 100X objective lens, using an Olympus IX83 inverted epifluorescence microscope. Single spores were segmented based on the phase-contrast image as described below in 'Single-spore tracking' and the resulting binary mask was used to measure APG-4 AM intensity for each spore.

3.5.5 Calibration of the intracellular potassium indicator APG-4 AM

A single *B. subtilis* colony was used to inoculate 5 mL of LB, and incubated 2 h in a shaking incubator at 37 °C (200 rpm). Then, 2 μM APG-4 AM were added to the media during the incubation time of 45 min. Following the incubation, cells were washed with MSgg media (5 mM potassium phosphate (pH 7.0), 100 mM 3-(N-morpholino)propanesulfonic acid (pH 7.0), 2 mM $MgCl_2$, 700 μM $CaCl_2$, 50 μM $MnCl_2$, 100 μM $FeCl_3$, 1 μM $ZnCl_2$, 2 μM thiamine, 0.5% glycerol, 0.5% glutamate) and incubated 1 h. Later, 10 μg.ml-1 valinomycin was added in the media for 1 h to equilibrate intracellular and extracellular potassium concentrations [66]. Following this treatment, we loaded cells in four independent chambers of the microfluidic device and exposed them to the addition of different extracellular potassium concentrations (0, 100, 200, and 400 mM KCl), respectively, and inoculated 1 h to stabilize. Phase contrast and fluorescence snapshot images were taken and analyzed for each condition, as described above.

3.5.6 Microfluidic germination assay with germinant pulses

For microfluidic culturing, we used the CellASIC ONIX Microfluidic Platform and Y04D microfluidic plates (EMD Millipore). Prepared spore suspension was loaded into the microfluidic chamber, and incubated for 1 h at 37 °C with RM supplied at 0.75 psi each from two wells for stabilization of the plate. After 1 h from the start of image acquisition, germinant pulses were delivered by switching to a well containing RM with 10 mM L-alanine for 3 min at 2.5 psi every 2 h. After the germinant pulse, RM was supplied from two wells at 2.5 psi each to wash the chamber before returning to the baseline condition of 0.75 psi. The 3-minute pulse duration was selected based on the consideration of our 5-minute imaging rate, to allow sufficient time for germinant introduction and removal in the device.

3.5.7 Microfluidic germination assay with potassium channel blocker

For experiments using the potassium blocker quinine (Figs. 3.3 and 3.4), spores were prepared as usual and loaded into a microfluidic plate. 1 mM quinine (MilliporeSigma, St. Louis, MO, USA) was added to all wells containing RM, including the wells with 10 mM L-alanine. Before starting the experiment, spores were incubated in the presence of quinine at 37 °C for 45 min to ensure the efficacy of the drug. The germination assay was done according to the germinant pulse method described above.

3.5.8 Time-lapse microscopy

Spore germination was monitored with phase-contrast microscopy using an Olympus IX83 inverted epifluorescence microscope. Images were taken with an Orca-Flash 4.0 LT+ camera (Hamamatsu) and an X-Cite Turbo light source (Excelitas Technologies) under a 100X objective lens. Spore images were taken every 1 or 5 mins.

3.5.9 Dyes and concentrations

Electrochemical potential dynamics were measured using the fluorescent cationic dyes Thioflavin-T (ThT) or Tetramethylrhodamine, Methyl Ester, Perchlorate (TMRM), both at a concentration of 10 μM. The charge-neutral version of Thioflavin-T (neutral ThT) was used at a concentration of 10 μM. The extracellular potassium indicator APG-4 TMA and the intracellular potassium indicator APG-4 AM were used at a concentration of 2 μM.

3.5.10 Synthesis of charge-neutral ThT

The synthesis of neutral ThT was accomplished using a modification of a reported procedure [67]. The spectroscopic and analytical data of the synthesized compound were identical to

those reported in the literature [68]. For the synthetic procedures and compound characterization see Fig. S3.9 and Appendix B.

3.5.11 Experimental reproducibility

Data shown in the main figures were drawn from a minimum of three independent experiments. For multiple strains or conditions in the same panel, such as Figs. 3.2G and 3.3H, head-to-head experiments with WT spores (separate chambers in the same microfluidic device) were done on the same day as a control.

3.5.12 Single-spore tracking

Single spores were tracked using a combination of Fiji plugins. The stage drift in time-lapse phase-contrast images was corrected using the MultiStackReg plugin. After drift correction, single dormant spores were segmented based on Otsu thresholding. Non-spore particles were discarded through size and shape filtering, and further manual inspection. The resulting binary mask was then used to measure the phase-contrast and fluorescence intensity of individual spores throughout the movie with the MultiMeasure plugin.

3.5.13 Determination of germination time

Phase-contrast intensity data acquired through the previous step was analyzed by custom-written software in Python to calculate the germination time for each spore. Based on the well-known phase-contrast darkening that indicates spore rehydration following germination initiation [34], we define germination time as the time where the phase-contrast intensity of the spore darkens beyond the background (Fig. S3.1A,B). Statistical analyses and data visualization were also performed by custom-written software in Python.

3.5.14 Calculation of germination probability and integration capacity

The germination probability for each pulse was calculated by dividing the number of spores that germinated in response to the pulse, by the number of remaining dormant spores before the pulse. Integration capacity was defined as the average pairwise difference of concurrent germination probabilities, calculated up to the pulse of half-maximum dormancy. The half-maximum dormancy was determined from the corresponding dormant fraction curves.

3.5.15 Calculation of change in electrochemical potential

Change in electrochemical potential (Fig. 3.4F,G) was calculated for each spore by normalizing the ThT value for each spore with its initial ThT value. The average potential change (Fig. 3.4H) was obtained by extracting an average ThT value over a 20-minute window between each germinant pulse to establish the baseline of each step-wise increase. Then, the difference between each step was calculated to obtain the step sizes. Finally, the average step size across all the spores was obtained, up to the pulse were half of the population remained dormant (half-maximum dormancy).

3.6 Acknowledgements

Chapter 3 is currently under review in the working citation: Kikuchi K, Galera-Laporta L, Weatherwax C, Lam JY, Moon E, Theodorakis EA, Garcia-Ojalvo J, Süel GM,“Electrochemical potential enables dormant spores to integrate environmental signals”. The dissertation author was a primary investigator and the first author of this material alongside Leticia Galera-Laporta. We acknowledge Munehiro Asally, Tolga Çağatay, Joseph Larkin, Colin Comerci, and Katherine Süel for helpful discussions; Wade Winkler and David Kearns for kindly providing bacterial strains; and Jacqueline Humphries for help with strain construction.

Figure 3.1 *(following page)*: *Bacillus subtilis* spores integrate over two consecutive germinant pulses.
(A) Bacterial spores can remain in dormancy (shaded area in blue) for years seemingly without any biological activity. It is thus unclear how spores sense environmental cues while dormant, and before triggering germination. **(B)**) Filmstrip from phase-contrast microscopy showing the fractional germination response to the pulses. Spores contained in a microfluidic chip were subjected to 3 min germinant pulses (10 mM L-alanine, dotted vertical lines) separated by 2-hour intervals. These pulses triggered germination of a subset of spores, detected by phase-contrast imaging: white dormant spores become phase dark when germinating as they rehydrate. Spores that maintain dormancy, despite exposure to germinant pulses, provoke the question of whether they can sense and process such environmental information. Scale bar indicates 5 μm. **(C)** Single-cell time traces showing the change in the normalized phase-contrast intensity during spore germination (n = 200, subset of data from Fig. 3.1D). We note that collective fluctuations in the image intensity are due to subtle changes in camera focus. **(D)** Fraction of dormant spores after each germinant pulse (n = 2,244). The abrupt decrease in the dormancy fraction after the second germinant pulse indicates a priming effect, or in other words the ability of spores to integrate signals over consecutive pulses. **(E)** The germination probability in each pulse is calculated based on the remaining dormant spores before each germinant pulse. The difference in the germination probability between the two pulses (vertical arrow) provides a metric to quantify the information integration by spores. **(F)** Cartoon showing the main components of our mathematical model. The flux of potassium in a spore is assumed to depend partially on the difference between its internal (K_i) and external (K_e) concentrations, the K-channel conductance (gk), and the membrane potential (V) of the spore. **(G)** The spore's approach to germination is dictated by initial potassium content (K_i) and potassium efflux. **(H)** In the mathematical model, the initial potassium content (K_i, t = 0) and the K-channel conductance (gk) determine the potassium dynamics in spores (K_i(t)). These dynamics determine the spore's ability to maintain dormancy (See Appendix B). **(I)** Simulated fraction of dormant spores after each germinant pulse.

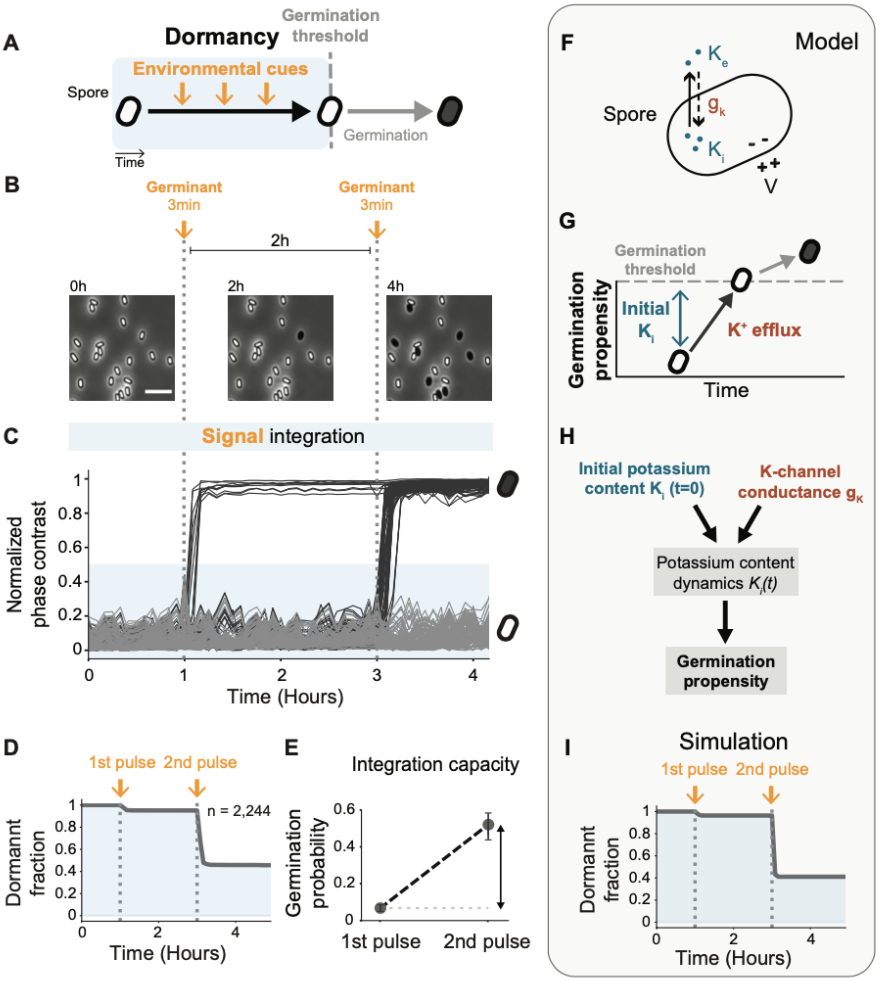
A
Dormancy
Germination threshold
Environmental cues
Spore
Germination
Time
B
Germinant 3min
Germinant 3min
2h
0h
2h
4h
C
Signal integration
Normalized phase contrast
Time (Hours)
D
1st pulse 2nd pulse
n = 2,244
Dormannt fraction
Time (Hours)
E
Integration capacity
Germination probability
1st pulse
2nd pulse
F
Model
Spore
V
G
Germination threshold
Germination propensity
Initial K_i
K+ efflux
Time
H
Initial potassium content K_i (t=0)
K-channel conductance g_K
Potassium content dynamics K_i(t)
Germination propensity
I
Simulation
1st pulse 2nd pulse
Dormannt fraction
Time (Hours)

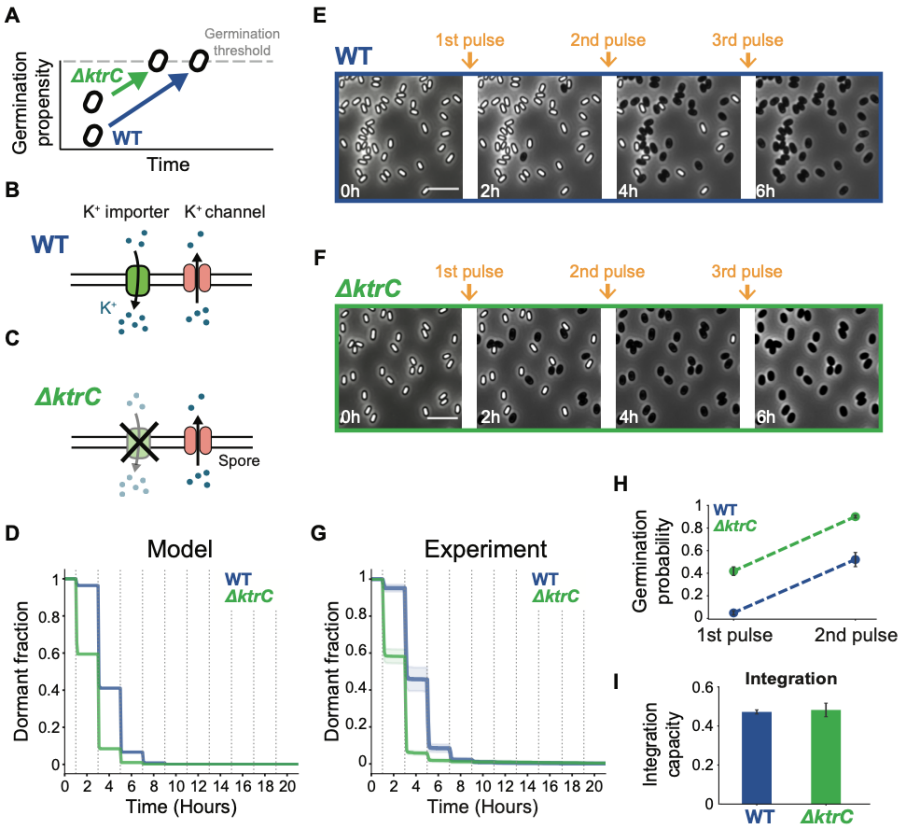

Figure 3.2: Role of potassium in the germination threshold.
(A) The model predicts that the deletion of the KtrC importer reduces the distance of spores to their germination threshold. This in turn will increase the germination propensity of Δ*ktrC* spores, compared to wild-type (WT) spores. **(B)** Wild-type cells contain both potassium importers and ion channels. **(C)** The ktrC mutant spores (Δ*ktrC*) lack the gene for the potassium importer KtrC. **(D)** Model-generated dormant fraction of the WT (blue), and the Δ*ktrC* (green) strains. Dotted vertical lines indicate germinant pulses. **(E&F)** Phase-contrast microscopy filmstrips for representative WT (E) and Δ*ktrC* spores (F), respectively. Snapshots show spores before and after the indicated germinant pulses. Scale bars indicate 5 μm. **(G)** Dormant fraction from single-cell experimental results for WT (blue, mean $\pm$ SD, n = 2,244, data from Fig. 3.1D), and Δ*ktrC* (green, mean $\pm$ SD, n = 2,154). Dotted vertical lines indicate germinant pulses. **(H)** germination probabilities of the WT and the Δ*ktrC* spores increase with consecutive pulses. Both strains reach 50% dormancy out of all initial spores (half-maximum dormancy) after two consecutive pulses. Error bars represent standard deviation. **(I)** Barplot showing the integration capacity of the WT and the Δ*ktrC* strains (0.47 $\pm$ 0.01 and 0.48 $\pm$ 0.03, respectively) calculated from the differences in germination probabilities shown in panel (H). Error bars represent standard deviation.

Figure 3.3 *(following page)*: Potassium ion flux underlies integration capacity of dormant spores.
(A) The Δ*yugO* mutant spores are expected to have be initially closer to the germination threshold but have slower potassium efflux, impacting their approach to the threshold. The inhibition of potassium channels in WT spores is similarly expected to impact their approach to the germination threshold. **(B)** The Δ*yugO* mutant spores lack the gene for the YugO channel, which is the only known potassium-specific channel in B. subtilis spores. **(C)** The drug quinine targets potassium channels, blocking ion efflux. **(D)** Model-generated dormant fraction of WT (blue), Δ*yugO* (red), and quinine addition to WT spores (purple). **(E-G)** Filmstrips for representative WT (E) and Δ*yugO* (F) spores, and WT spores in the presence of 1 mM quinine (G), respectively. Snapshots show spores before and after the indicated germinant pulses. Scale bars indicate 5 μm. **(G)** The dormant fraction from single-cell measurements of WT (mean ± SD; blue, n = 2,244, data from Fig. 3.1D), Δ*yugO* (mean ± SD; red, n = 1,058), and 1 mM quinine addition to WT spores (mean ± SD, purple, n = 4,491). **(H)** Germination probabilities of the WT and the Δ*ktrC* spores increase with consecutive pulses. Both strains reach 50% dormancy out of all initial spores (half-maximum dormancy) after two consecutive pulses. Error bars represent standard deviation. **(I)** The germination probability until half-maximum dormancy for WT (data from Fig. 3.2H), Δ*yugO*, and quinine addition. The inhibition of potassium efflux reduces the germination probability, requiring three pulses to reach the half-maximum dormancy. Error bars represent standard deviation. **(J)** The genetic and chemical inhibition of potassium efflux (Δ*yugO* and quinine addition, respectively) reduces the integrative capacity of spores (WT 0.47 ± 0.01, data from Fig. 3.2I, Δ*yugO* 0.17 ± 0.04, and quinine 0.18 ± 0.01; mean ± SD).

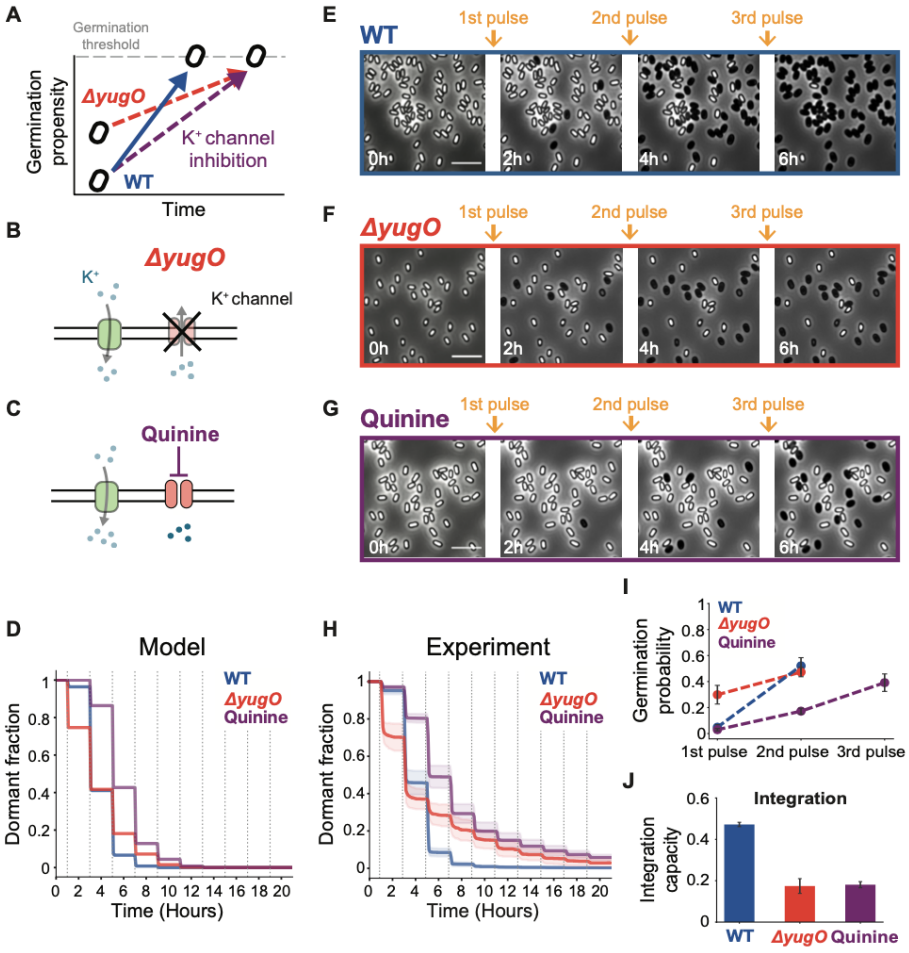
A
Germination threshold
Germination propensity
ΔyugO
WT
K⁺ channel inhibition
Time
B
ΔyugO
K⁺
K⁺ channel
C
Quinine
D
Model
WT
ΔyugO
Quinine
Dormant fraction
Time (Hours)
E
WT
1st pulse
2nd pulse
3rd pulse
0h
2h
4h
6h
F
ΔyugO
G
Quinine
H
Experiment
I
Germination probability
1st pulse 2nd pulse 3rd pulse
J
Integration
Integration capacity

Figure 3.4 *(following page)*: Dormant spores exhibit sudden changes in their electrochemical potential, visualizing integration over germinant pulses.
(A) Cartoon illustrating the hypothesis that spores release potassium after each germinant pulse, generating a change in their electrochemical potential. **(B)** Mathematically predicted stepwise membrane potential (mV) jumps when spores are exposed to germinant pulses (dotted vertical lines). Depicted are representative time traces for individual spores that germinate in response to different germinant pulse numbers. The termination of the time trace indicates germination. **(C)** Phase-contrast images of a spore that remains dormant (phase bright) despite exposure to three consecutive germinant pulses. Dotted vertical lines indicate germinant pulse exposure. Scale bar indicates 1 μm. **(D)** Top fluorescence filmstrip shows the color-coded electrochemical potential amplitude (ThT, a.u.) of the spore depicted in panel (C). The other three filmstrips below show individual spores, each of which germinate in response to different germinant pulses. **(E)** Single-cell time traces of the electrochemical potential signal (ThT, a.u.) for the corresponding spores in Fig. 3D (see Fig. S3.7A for corresponding phase-contrast traces). The termination of the time traces indicates germination. The inset shows the time trace of a single spore stained with the charge-neutral ThT fluorescent dye (see Fig. S3.8D for data from multiple spores). **(F)** Measurement of 3,484 individual WT spores showing amplitude color-coded time traces that show the changes in electrochemical potential signal (ThT, a.u.) triggered by germinant pulses (dotted vertical lines). The termination of the time trace (white region) indicates germination. **(G)** Single-cell time traces of the potential change (ThT, a.u) for Δ*ktrC* (n = 8,790), Δ*yugO* (n = 2,380), and WT with 1 mM quinine (n = 3,653), respectively. Each line represents a single-spore time trace until germination (white region). Germinant pulses are indicated with arrows and dotted vertical lines. **(H)** Scatter plot of the integration capacity as a function of the average potential change (ThT, a.u) of all strains and conditions tested in this study: WT, Δ*ktrC*, Δ*yugO*, and WT with quinine. **(I)** Conceptual summary of the proposed integrate-and-fire mechanism. Spores integrate germinant exposure information over time through efflux of potassium ions. The resulting change in electrochemical potential drives them towards a germination threshold. Spores that reach the threshold "fire" the germination program which is marked by the abrupt change in phase-contrast refractility.

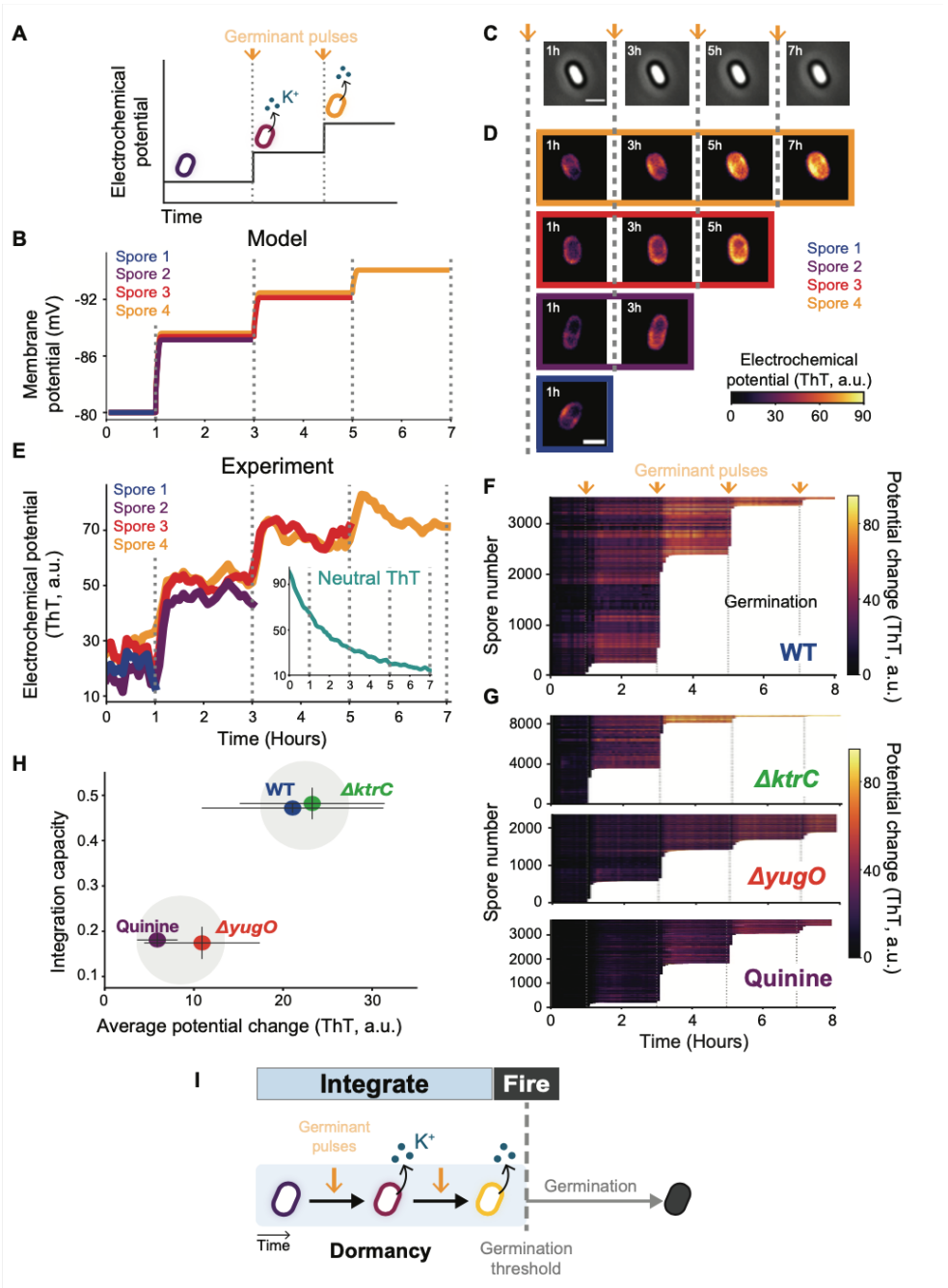
A
Germinant pulses
Electrochemical potential
K+
Time
B
Model
Spore 1
Spore 2
Spore 3
Spore 4
Membrane potential (mV)
-92
-86
-80
0 1 2 3 4 5 6 7
C
1h
3h
5h
7h
D
Spore 1
Spore 2
Spore 3
Spore 4
Electrochemical potential (ThT, a.u.)
0 30 60 90
E
Experiment
Spore 1
Spore 2
Spore 3
Spore 4
Electrochemical potential (ThT, a.u.)
Neutral ThT
Time (Hours)
F
Germinant pulses
Spore number
Germination
WT
Potential change (ThT, a.u.)
G
ΔktrC
ΔyugO
Quinine
Spore number
Time (Hours)
Potential change (ThT, a.u.)
H
WT
ΔktrC
Quinine
ΔyugO
Integration capacity
Average potential change (ThT, a.u.)
I
Integrate
Fire
Germinant pulses
K+
Germination
Time
Dormancy
Germination threshold

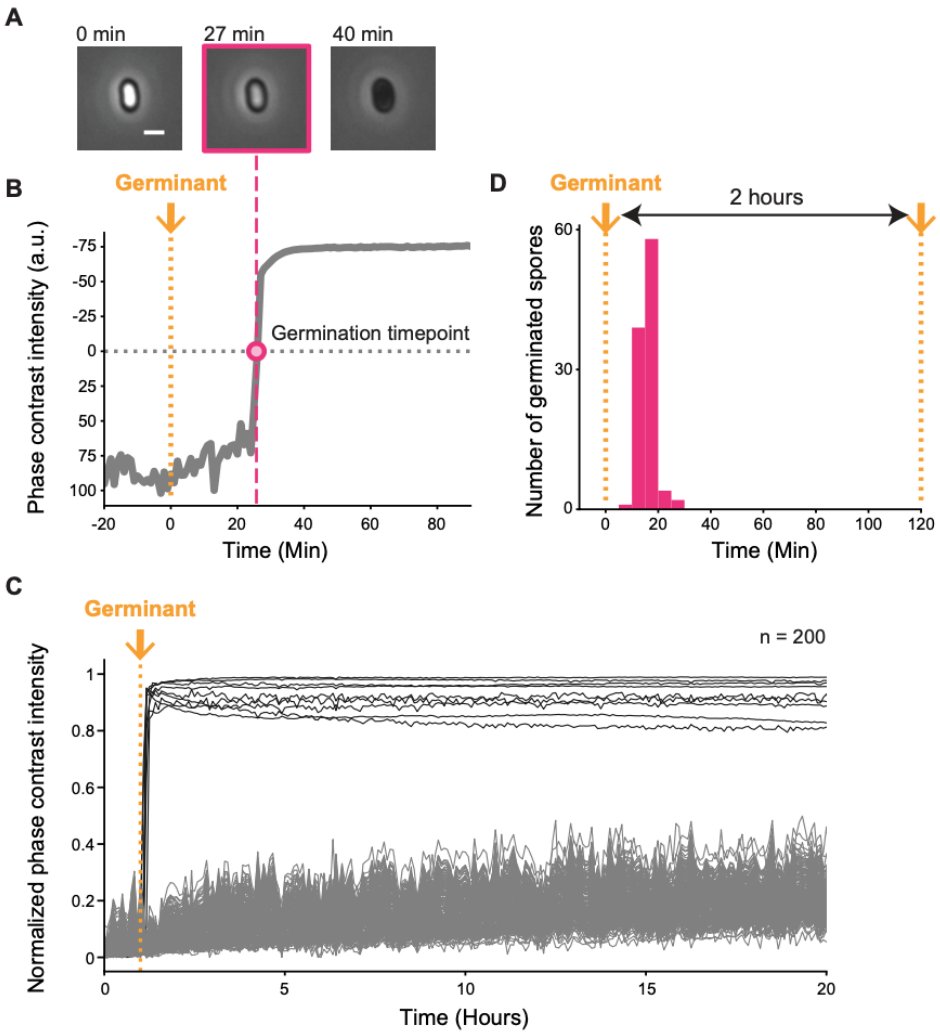

Figure S3.1: Germination dynamics of spores in response to a single germinant pulse. **(A)** Filmstrip of a representative germinating wild-type (WT) spore. The snapshot bordered in magenta corresponds to the timepoint where the spore is considered to germinate (germination timepoint). Scale bar indicates 1 μm. **(B)** Corresponding single-cell time trace of the spore in panel A showing phase-contrast intensity (a.u.). After subtracting the background signal, the germination timepoint (magenta circle) is detected as the timepoint where the phase contrast intensity goes below zero. The 3-minute pulse of germinant (10 mM L-alanine) is indicated with a dotted vertical line. **(C)** Normalized phase-contrast intensity time traces of WT spores exposed to a single germinant pulse (n = 200). Notice that changes in camera focus create global changes of phase-contrast values. **(D)** Histogram of germination timepoints in response to a single 3-minute germinant pulse (14.68 ± 0.66 minutes, n = 104). Data from Fig. 3.1D.

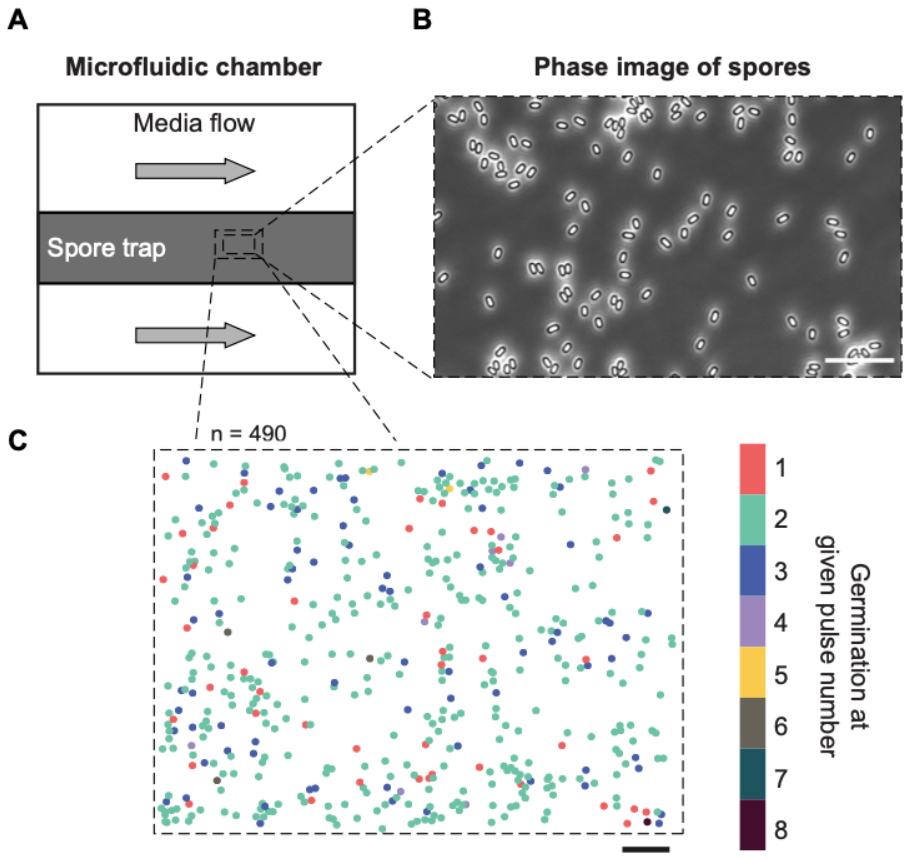

Figure S3.2: Germination does not correlate with spatial position within the microfluidic chamber.
(A) Cartoon illustrating the microfluidic chamber used in this study. Spores are trapped in a chamber with media flow on each side. **(B)** A representative snapshot of WT spores in the spore trap. Scale bar indicates 10 μm. **(C)** Plot showing WT spores in their respective locations within the spore trap. Colors correspond to the germinant pulse number in which they germinated. Scale bar indicates 10 μm.

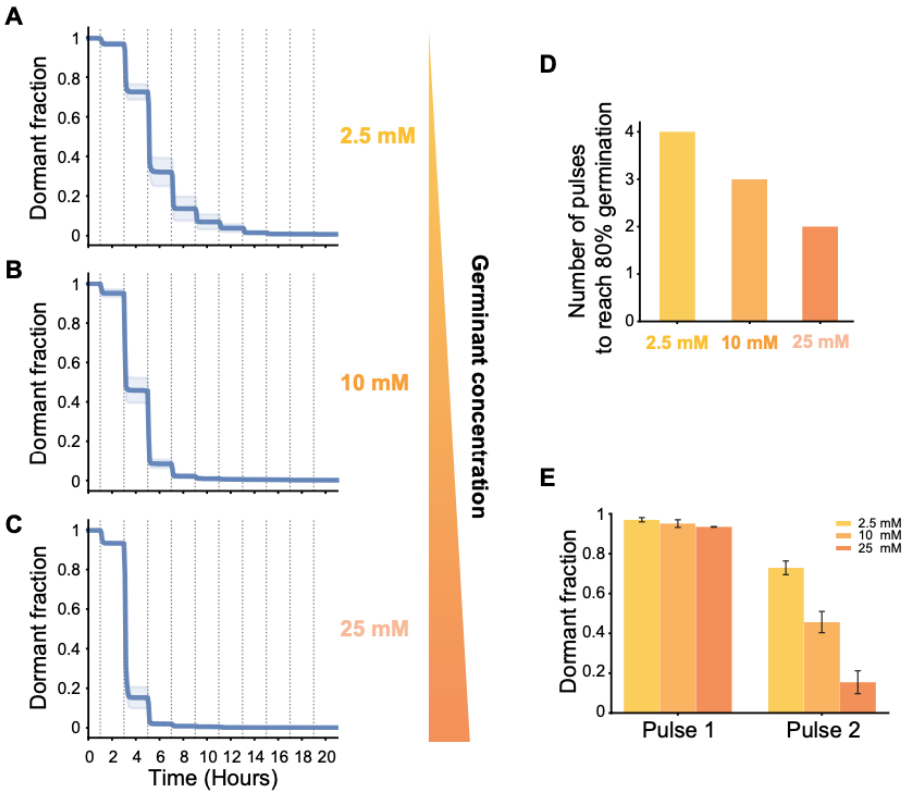

Figure S3.3: The sensitivity of spores to different concentrations of germinant supports the integrate-and-fire model.
(A-C) Dormant fraction cumulative distribution functions (CDFs) of WT spores subjected to pulses of 2.5, 10, and 25 mM L-alanine (2.5 mM, n = 3,794; 10 mM, n = 2,244, data from Figure 2G; 25 mM, n = 2,668). For all cases, the interval between pulses is 2 h. **(D)** The bar plot indicates the number of germinant pulses required to reach 80% germination. Data from panels A-C. **(E)** The bar plot indicates the dormant fraction for each condition after the 1st and 2nd pulses. Data from panels A-C. Error bars represent standard deviation.

Figure S3.4 *(following page)*: Potassium measurements in dormant spores using fluorescent indicators.
(A) Structure of the extracellular potassium indicator APG-4 TMA. **(B)** Average fluorescent time traces from single WT spores stained with 2 μM of the extracellular potassium indicator APG-4 TMA, without (orange, n = 20) or with 1 mM quinine addition (purple, n = 24). The 3-minutes pulse of germinant (10 mM L-alanine) is indicated with vertical dotted lines. Shaded regions represent standard deviation. Data was normalized to 1 at the 1-hour mark. All spores remained dormant during the timescale shown in the plot. **(C)** Structure of the intracellular potassium indicator APG-4 AM. **(D)** Representative fluorescence snapshots of WT, Δ*yugO*, and Δ*ktrC*spores stained with the intracellular potassium indicator APG-4 AM. Scale bars indicate 1 μm. **(E)** Average fluorescence intensities of dormant WT (blue, n=1,037), Δ*yugO* (red, n=776), and Δ*ktrC*(green, n=1,107) spores that were generated in the presence of 2 μM APG-4 AM. Both Δ*yugO* and Δ*ktrC*intensities were significantly lower compared to WT (p¡1*10-14, two sample Kolmogorov-Smirnov test). Error bars indicate SEM. **(F)** Calibration curve for the intracellular potassium fluorescence indicator APG-4 AM. The black data points indicate APG-4 AM measurements for cells exposed to the addition of different KCl concentrations (0, 100, 200, and 400 mM KCl). Error bars indicate standard deviation. The mean values for dormant WT, Δ*yugO*, and Δ*ktrC*spores are indicated with the dotted lines (data from panel D).

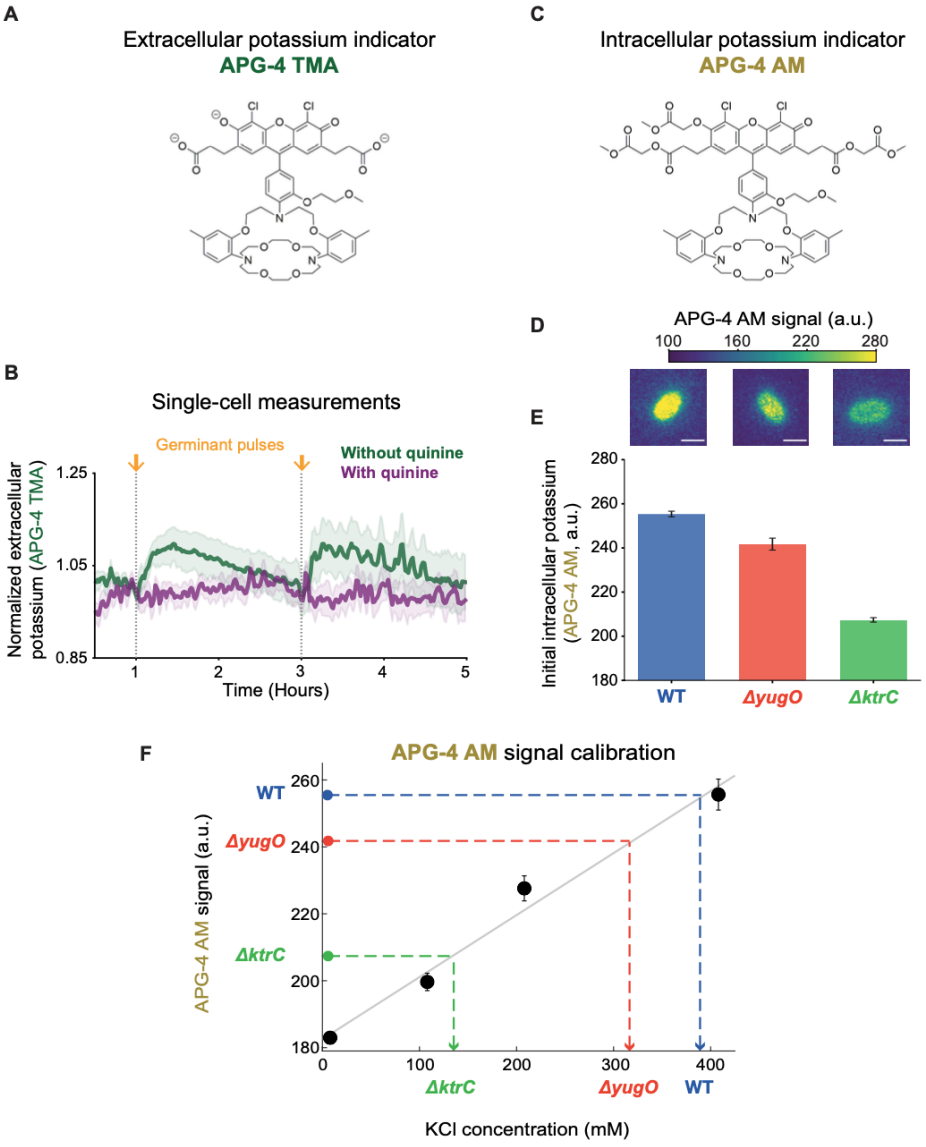
A
Extracellular potassium indicator
APG-4 TMA
C
Intracellular potassium indicator
APG-4 AM
B
Single-cell measurements
Germinant pulses
Without quinine
With quinine
Normalized extracellular potassium (APG-4 TMA)
1.25
1.05
0.85
1
2
3
4
5
Time (Hours)
D
APG-4 AM signal (a.u.)
100
160
220
280
E
Initial intracellular potassium (APG-4 AM, a.u.)
280
260
240
220
200
180
WT
ΔyugO
ΔktrC
F
APG-4 AM signal calibration
APG-4 AM signal (a.u.)
260
240
220
200
180
WT
ΔyugO
ΔktrC
0
100
200
300
400
ΔktrC
ΔyugO
WT
KCl concentration (mM)

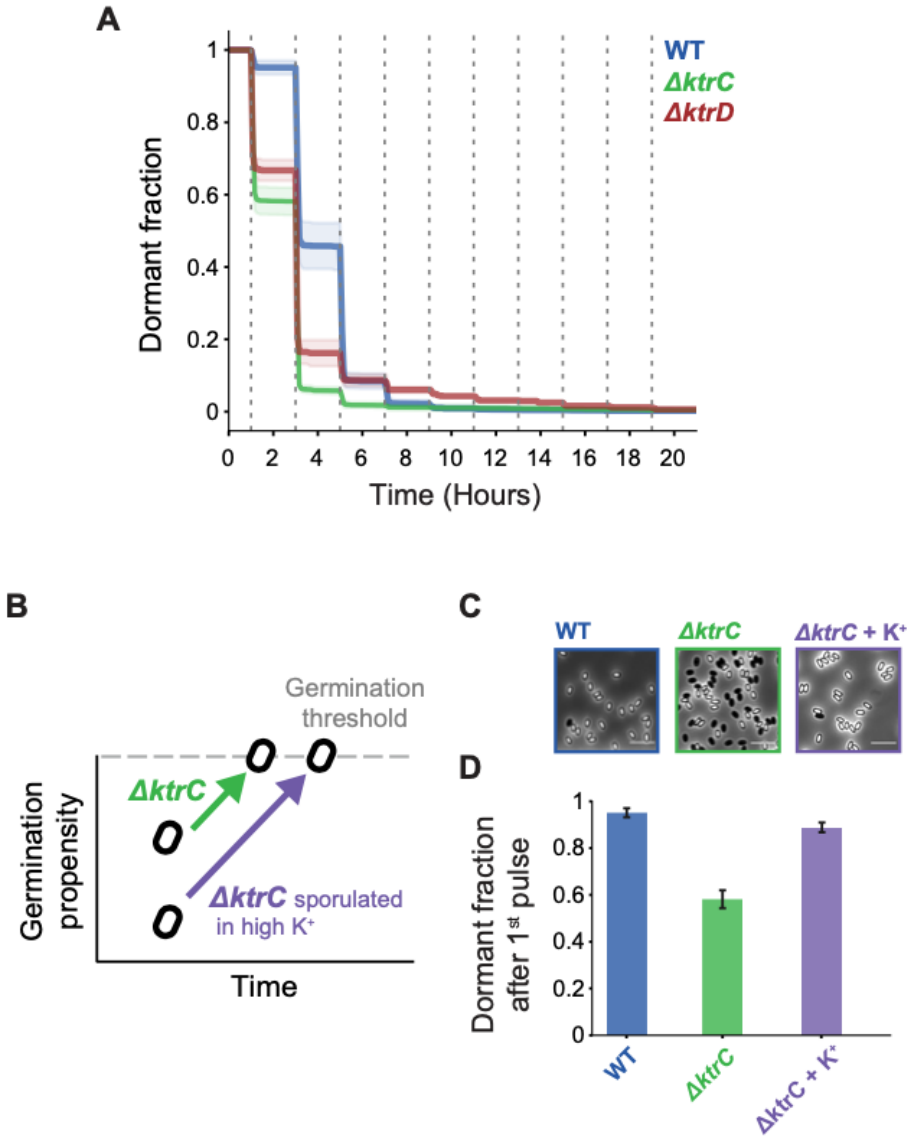

Figure S3.5: Rescue of the Δ*ktrC* phenotype confirms that intracellular potassium concentrations determine the distance to the germination threshold.
(A) Dormant fraction for single-cell experiment results for WT (blue, mean ± SD, n = 2,244, data from Fig. 3.1D), Δ*ktrC*(green, mean ± SD, n = 2,154, data from Fig. 3.3G), and Δ*ktrD* (brown, mean ± SD, n = 442). The dotted vertical lines indicate timepoints where 3-minute pulses of 10 mM L-alanine were applied. **(B)** Cartoon illustrating that higher potassium concentration in the sporulation medium increases the distance of Δ*ktrC*spores to the germination threshold, rescuing the Δ*ktrC* phenotype. **(C)** Snapshots for representative WT, Δ*ktrC*, and Δ*ktrC* spores with 150 mM potassium addition during sporulation. Snapshots show spores after the 1st germinant pulse. Scale bars indicate 5 μm.

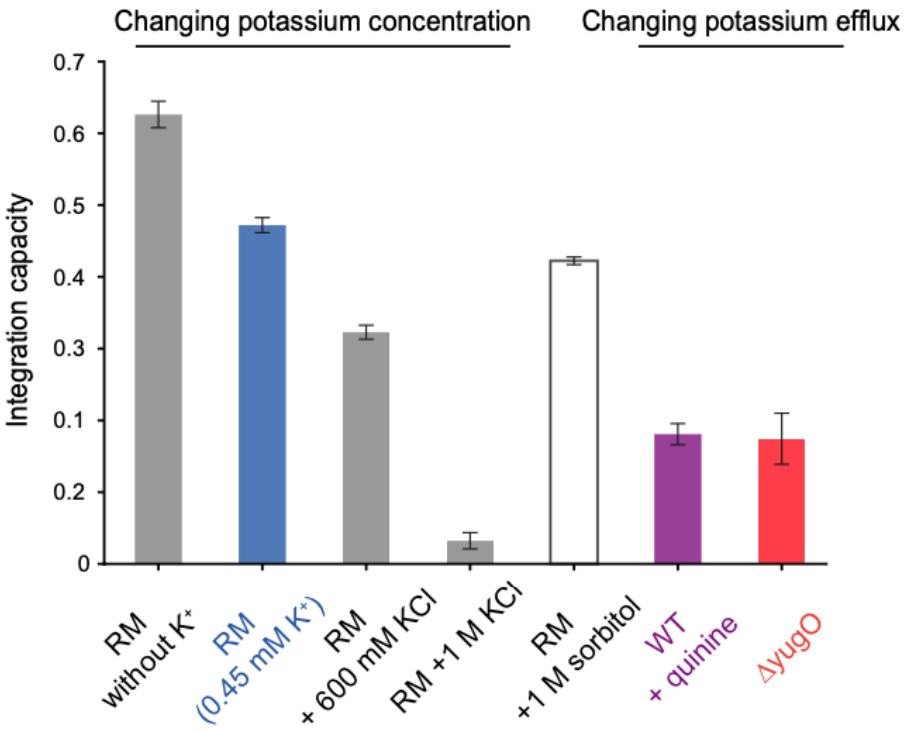

Figure S3.6: Modulation of potassium efflux recapitulates Δ*yugO* phenotype.
Integration capacities of WT spores (n = 2,244, data from Fig. 3.1D), WT spores in various external KCl concentrations (RM without K+, n = 903; 600 mM, n = 1,061; 1 M, n = 1,699), WT spores in presence of 1 M sorbitol (n = 2,819), WT spores in presence of 1 mM quinine (n = 4491, data from Fig. 3.3J), and Δ*yugO* spores (n = 1,058, data from Fig. 3.3J). Error bars indicate standard deviation.

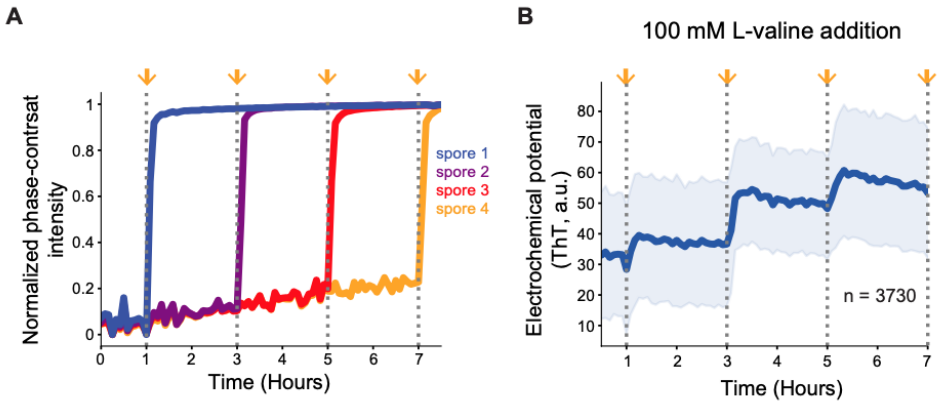

Figure S3.7: Phase contrast of spores during germinant pulses and ThT dynamics in response to L-valine pulses.
(A) Single-cell time traces of min-max normalized phase-contrast intensity for spores shown in Fig. 3.4D and E. Notice that changes in camera focus create global changes of phase-contrast values. The dotted vertical lines indicate timepoints where 3-minute pulses of 10 mM L-alanine were applied. **(B)** Mean fluorescence time trace of WT spores stained with 10 μM ThT (mean ± SD, n = 3,730). The dotted vertical lines indicate timepoints where 3-minute pulses of 100 mM L-valine were applied. The shaded area corresponds to the standard deviation.

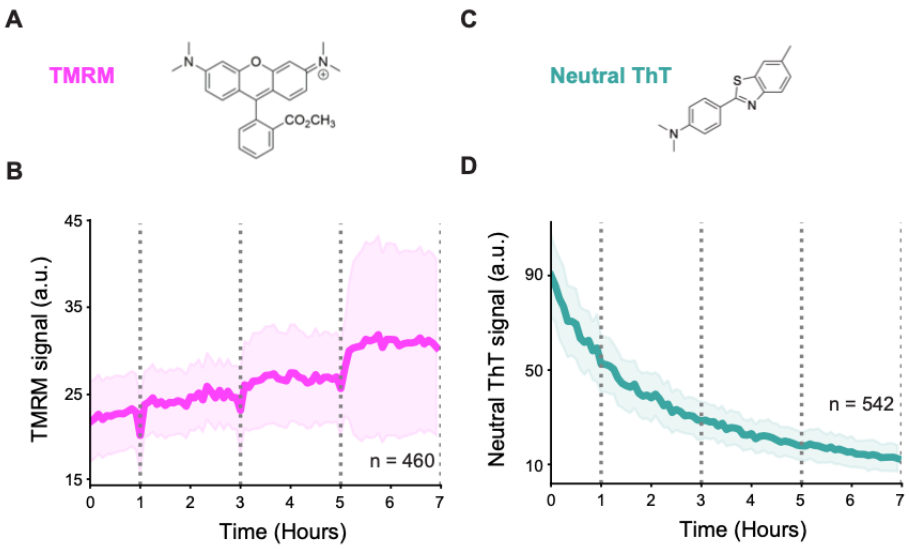

Figure S3.8: Comparison of charged and uncharged electrochemical potential reporter dyes. **(A)** Chemical structure of the cationic fluorescent dye Tetramethylrhodamine methyl ester (TMRM). **(B)** Mean fluorescence time trace of WT spores stained with 10 μM TMRM (mean ± SD, n = 460). The mean is calculated from fluorescence values before each spore's germination timepoint. The shaded area corresponds to standard deviation. **(C)** Chemical structure of the charge-neutral ThT. **(D)** Mean fluorescence time trace of WT spores stained with 10 μM neutral ThT (mean ± SD, n = 542). The mean for all germinated spores shows a decrease in signal likely due to photobleaching. The shaded area corresponds to standard deviation.

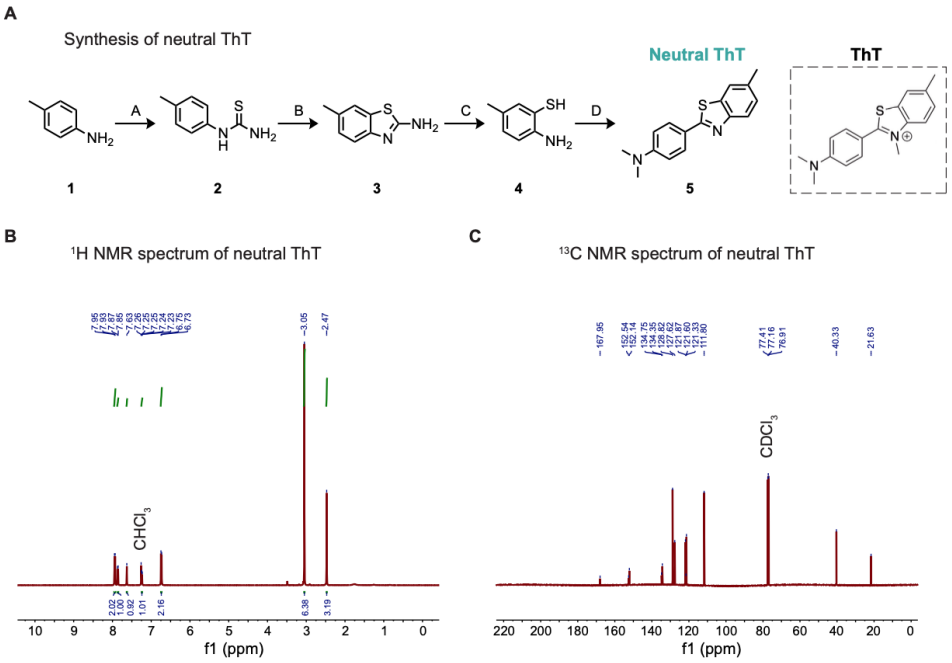

Figure S3.9: Synthesis and characterization of neutral ThT.
(A) Intermediates for the synthesis of neutral ThT: (1) p-toluidine, (2) 1-(p-tolyl)thiourea, (3) 6-methylbenzo[d]thiazol-2-amine, (4) 2-amino-5-methylbenzenethiol, (5) N,N-dimethyl-4-(6-methylbenzo[d]thiazol-2-yl)aniline ("neutral ThT"). Reactions and conditions: (A) 1.0 equiv 1, 1.1 eq NH_4SCN, 27% aq. H_2SO_4, 20h, 85 °C, 61%; (B) 1.0 equiv 2, 0.1 equiv HBr, conc. H_2SO_4, 2h, 80 °C, 57%; (C) 1.0 equiv 3, 40% NaOH, 20h, 100 °C, 31%; (D) 1.0 equiv p-dimethylaminobenzaldehyde, 1.2 equiv 4, cat. amberlite IR-120, EtOH, mw irradiation, 3h, 100 °C, 40%. **(B)** ^{1}H Nuclear Magnetic Resonance (NMR) spectrum of neutral ThT. The observed signals correspond to the protons in neutral ThT and are used to confirm the chemical structure. Green lines represent the integration (number of protons corresponding to each signal, annotated under the peaks). The signal for the solvent ($CHCl_3$) is at 7.26 ppm. **(C)** ^{13}C NMR spectrum of neutral ThT. The observed signals correspond to the carbons in neutral ThT and are used to confirm the chemical structure. The signal for the solvent ($CDCl_3$) is at 77.41, 77.16, and 76.91 ppm.

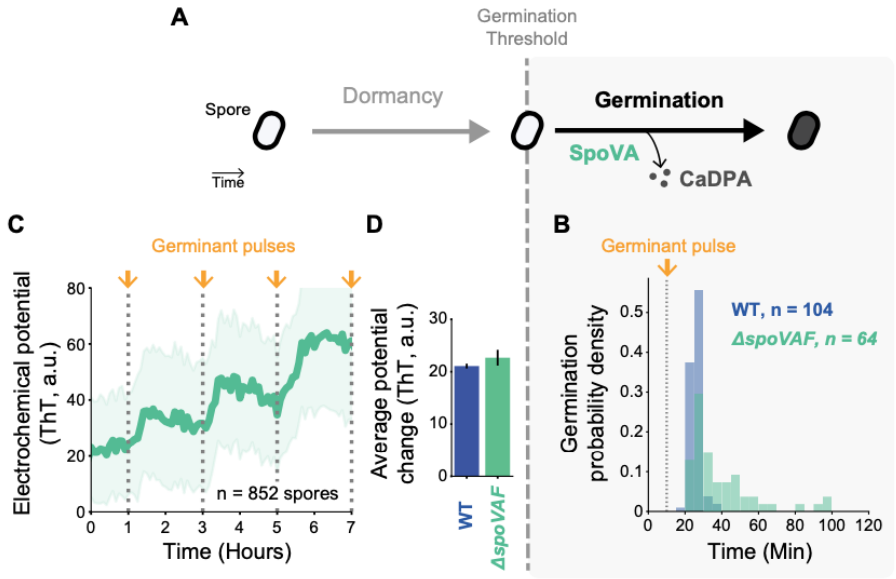

Figure S3.10: Deletion of the SpoVAF subunit of the SpoVA CaDPA channel does not affect electrochemical dynamics in dormant spores.
(A) Cartoon illustrating the efflux of CaDPA through the SpoVA channel, a well-known process in the germination program following germination. **(B)** Normalized histogram of germination time in response to a single germinant pulse for WT (n = 104, data from Fig. 3.1D and S3.1D) and Δ*spoVAF* (n = 64) spores. **(C)** Mean fluorescence time trace of dormant Δ*spoVAF* spores stained with 10 μM ThT (n = 852). The dotted vertical lines indicate 3-min pulses of 10 mM L-alanine. The shaded area corresponds to standard deviation. **(D)** Bar plots indicating average electrochemical potential change of WT (n = 3,484, data from Fig 3.4F) and Δ*spoVAF* (n = 852, data from panel C) spores. Error bars represent 99% confidence intervals.

Table S3.1: *Bacillus subtilis* strains used in Chapter 3.

Strain	Genotype	Source
Wild type	*B. subtilis* NCIB 3610	Gift from Wade Winkler laboratory (University of Maryland, College Park, MD)
Δ*yugO*	*yugO*:: neo	Laboratory collection
Δ*ktrC*	*ktrC*:: spec	This study
Δ*ktrD*	*ktrD*:: tet	Gift from Daniel Kearns laboratory (Indiana University Bloomington, IN)
Δ*spoVAF*	*spoVAF*:: spec	This study

Chapter 4

Conclusion and Closing Remarks

In this dissertation, I described two studies that examine how bacteria transmit and process signals using ions and electrochemical charges. In Chapter 2, we saw how single bacterial cells within biofilms are spatially organized to optimize signal transmission, and in Chapter 3, we made the first foray into understanding how signal processing is driven in metabolically dormant spores. I hope to have conveyed the sense of wonder that comes from seeing cells employ these surprisingly sophisticated and elegant mechanisms, and cannot wait to see what future research will uncover in this field.

Appendix A

Mathematical model for Chapter 3

A.1 Hodgkin-Huxley based potassium flux model

To describe the effect of potassium efflux on spore germination, we developed a Hodgkin-Huxley-based model of potassium flux in a dormant spore. We consider the germination event to be when the internal potassium concentration of the spore decreases below a certain threshold K_s. We assume that the initial potassium levels of a spore population follow a normal distribution.

Potassium ions can cross the spore membrane through ion channels. Potassium flux across the membrane depends on the fraction of ion channels that are open (n), the potassium ion concentration gradient, and the membrane potential of the spore (V), similar to a previously described model of potassium flux [2]. We explicitly modeled the dynamics of the intracellular and local extracellular potassium concentrations, K_i and K_e, respectively:

$$\frac{dK_e}{dt} = Fg_K n^4(V - V_K) + Fg_n n^4(V - V_n) - \gamma_e(K_e - K_m) \tag{A.1}$$

$$\frac{dK_i}{dt} = -Fg_K n^4(V - V_K) - Fg_n n^4(V - V_n) \tag{A.2}$$

Potassium can enter and leave the spore through both dedicated potassium channels and nonspe-

cific ion channels. The first term in both equations describes potassium flux through potassium ion channels, and the second term describes potassium flux through nonspecific ion channels. The nonspecific ion Nernst potential is approximated by the parameter V_n, and the potassium Nernst potential V_K is given by the equation:

$$V_K = V_{K0} \ln (K_e/K_i) \tag{A.3}$$

The dynamics of the spore's membrane potential is described by the following ordinary differential equation:

$$\frac{dV}{dt} = -g_K n^4 (V - V_K) - g_n n^4 (V - V_n) \tag{A.4}$$

The ion channels are assumed to effectively have four subunits, which can be in an open or closed position. The fraction of subunits n that are in the open position is described by the following equation, where the first term represents the opening of the channels due to germinant exposure and the second term represents their closing:

$$\frac{dn}{dt} = \alpha(1-n) - \beta n \tag{A.5}$$

When germinant is not present, $\alpha = 0$; otherwise, $\alpha = \alpha_g$. As a consequence, in the absence of germinant, the entire system is at steady state with channels closed, reflecting the idea that spores are dormant and stable.

A.2 Modeling genetic and chemical perturbations

We assume that cells lacking KtrC are less able to actively transport potassium into the cell than wild-type cells. Therefore, we assumed that Δ*ktrC* spores have lower average intracellular potassium levels than wild-type spores. Consequently, the starting membrane potential for Δ*ktrC*

spores is more negative than for wild-type spores.

Cells lacking the YugO channel have a potassium channel conductance of 0, or $g_K = 0$. Potassium ions can only enter or leave the Δ*yugO* spore through the nonspecific ion channels, which have a much lower conductance for potassium, so potassium efflux is slower than in wild-type spores. In addition, Δ*yugO* spores have less intracellular potassium than wild-type spores, and correspondingly a slightly more negative membrane potential. Finally, we assume that Δ*yugO* cells are less able to regulate potassium levels before and during sporulation, thus causing the distribution of initial intracellular potassium levels to be more variable than those of wild-type cells.

Quinine is assumed to decrease channel conductance, to g_{Kq} and g_{nq} for potassium channels and nonspecific ion channels, respectively.

Appendix B

Chemical synthesis procedures for Chapter 3

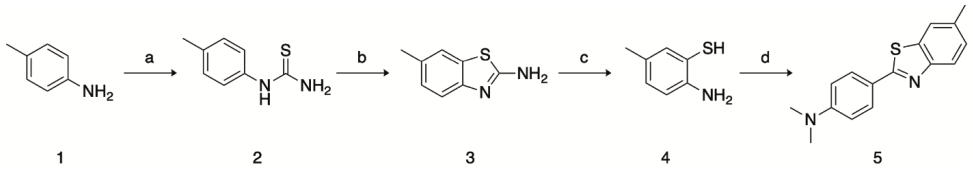

Figure B.1: Reactions and conditions for the synthesis of Neutral ThT. (a) 1.0 equiv (1), 1.1 eq NH_4SCN, 27% aq. H_2SO_4, 20 h, 85 °C, 61%; (b) 1.0 equiv (2), 0.1 equiv HBr, conc. H_2SO_4, 2 h, 80 °C, 57%; (c) 1.0 equiv (3), 40% NaOH, 20h, 100 °C, 31%; (d) 1.0 equiv p-dimethylaminobenzaldehyde, 1.2 equiv (4), cat. amberlite IR-120, EtOH, mw irradiation, 3 h, 100°C, 40%.

1-(p-tolyl)thiourea (2) [69]: To an aqueous solution of H_2SO_4 (27%, 10.0 mL) was added in one portion commercially available p-toluidine (1) (5.00 g, 46.66 mmol, 1.0 equiv.) and ammonium thiocyanate (3.91 g, 51.33 mmol, 1.1 equiv.). The reaction was allowed to stir overnight at 85 °C. Upon completion (tlc monitoring), toluene (10.0 mL) was added and the reaction mixture was refluxed for ^{1}H. The solution was neutralized with NH4OH and filtered to yield compound (2) as a white solid (61% yield). R_f = 0.35 (1:9 EtOAc:DCM); ^{1}H NMR (300 MHz, $CDCl_3$): δ 7.87 (bs, ^{1}H), 7.24 (d, J = 8.2 Hz, 2H), 7.12 (d, J = 8.3 Hz, 2H), 6.03 (bs, 2H), 2.37 (s, 3H). [70] 6-methylbenzo[d]thiazol-2-amine (3) [69]: To a solution of 2 (2.00

g, 12.03 mmol, 1.0 equiv.) in conc. H_2SO_4 (4.0 mL) was added slowly 48% HBr (0.08 mL, 1.20 mmol, 0.1 equiv.). The reaction was allowed to stir at 80 °C for 2 h. The reaction was diluted with cold water, neutralized with NH4OH and extracted with EtOAc (3 x 15.0 mL) to afford (3) as a pale-yellow solid (57% yield). R_f = 0.10 (1:9 EtOAc:DCM); ^{1}H NMR (300 MHz, $CDCl_3$): δ 7.44 (d, J = 8.19, ^{1}H), 7.41-7.40 (m, ^{1}H), 7.12 (dq, J = 8.2, 0.6 Hz, ^{1}H), 5.07 (bs, 2H), 2.40 (s, 3H). 2-amino-5-methylbenzenethiol (4) [71]: To a solution of 40% NaOH (12.5 mL) was added (3) (1.00 g, 6.09 mmol, 1.0 equiv.) and the reaction was heated at 100 °C for 20h. Upon completion (tlc monitoring), the solution was neutralized with AcOH then filtered to yield compound 4 as an off-white solid (31% yield). R_f = 0.75 (100% EtOAc); ^{1}H NMR (300 MHz, $CDCl_3$): δ 6.99-6.95 (m, 2H), 6.64 (d, J = 7.9 Hz, ^{1}H), 4.18 (s, 2H), 2.13 (s, 3H). [72] N,N-dimethyl-4-(6-methylbenzo[d]thiazol-2-yl)aniline (Neutral ThT, 5) [73]: To a 5.0 mL microwave vial was added p-dimethylamino benzaldehyde (0.05 g, 0.34 mmol, 1.0 equiv.) and 4 (0.05 g, 0.40 mmol, 1.2 equiv.) in EtOH (3.0 mL). A few beads of Amberlite IR-120 were added, and the reaction was subjected to microwave radiation at 100 °C for 3h. The precipitate was collected via filtration to provide (5) as a pale yellow solid (40% yield); R_f = 0.85 (1:9 EtOAc:DCM); ^{1}H NMR (500 MHz, $CDCl_3$): δ 7.94 (d, J = 8.9 Hz, 2H), 7.86 (d, J = 8.3 Hz, ^{1}H), 7.63 (s, ^{1}H), 6.25 (dd, J = 0.8, 8.6 Hz, ^{1}H), 6.74 (d, J = 8.9 Hz, 2H), 3.05 (s, 6H), 2.47 (s, 3H); 13C NMR (125 MHz, $CDCl_3$): δ: 167.95, 152.54, 152.14, 134.75, 134.35, 128.82, 127.62, 121.87, 121.60, 121.33, 111.80, 40.33, 21.63; HRMS (ESI-TOF) calculated for [$C_16H_17N_2S$]+ [M+H]+: 269.1107; found 269.1106 [68].

Bibliography

[1] J. Liu, A. Prindle, J. Humphries, M. Gabalda-Sagarra, M. Asally, D.-y. D. Lee, S. Ly, J. Garcia-Ojalvo, and G. M. Süel, "Metabolic co-dependence gives rise to collective oscillations within biofilms," *Nature*, vol. 523, no. 7562, p. 550, 2015.

[2] A. Prindle, J. Liu, M. Asally, S. Ly, J. Garcia-Ojalvo, G. M. Suel, and G. M. Süel, "Ion channels enable electrical communication in bacterial communities," *Nature*, vol. 527, no. 7576, 2015.

[3] D. Debanne, E. Campanac, A. Bialowas, E. Carlier, and G. Alcaraz, "Axon Physiology," *Physiological Reviews*, vol. 91, pp. 555–602, Apr. 2011.

[4] M. Notaguchi and S. Okamoto, "Dynamics of long-distance signaling via plant vascular tissues," *Frontiers in Plant Science*, vol. 6, 2015.

[5] C. M. Waters and B. L. Bassler, "QUORUM SENSING: Cell-to-Cell Communication in Bacteria," *Annual Review of Cell and Developmental Biology*, vol. 21, no. 1, pp. 319–346, 2005.

[6] B. Li and L. You, "Predictive power of cell-to-cell variability," *Quantitative Biology*, vol. 1, pp. 131–139, June 2013.

[7] A. Raj and A. van Oudenaarden, "Nature, nurture, or chance: Stochastic gene expression and its consequences," *Cell*, vol. 135, no. 2, pp. 216–226, 2008.

[8] O. Symmons and A. Raj, "What's Luck Got to Do with It: Single Cells, Multiple Fates, and Biological Nondeterminism," *Molecular Cell*, vol. 62, pp. 788–802, June 2016.

[9] S. Alonso and M. Bär, "Reentry produced by small-scale heterogeneities in a discrete model of cardiac tissue," *Journal of Physics: Conference Series*, vol. 727, p. 012002, June 2016.

[10] J.-M. Cao, Z. Qu, Y.-H. Kim, T.-J. Wu, A. Garfinkel, J. N. Weiss, H. S. Karagueuzian, and P.-S. Chen, "Spatiotemporal Heterogeneity in the Induction of Ventricular Fibrillation by Rapid Pacing: Importance of Cardiac Restitution Properties," *Circulation Research*, vol. 84, pp. 1318–1331, June 1999.

[11] B. E. Steinberg, L. Glass, A. Shrier, and G. Bub, "The role of heterogeneities and intercellular coupling in wave propagation in cardiac tissue," *Philosophical Transactions of the Royal Society A: Mathematical, Physical and Engineering Sciences*, vol. 364, pp. 1299–1311, May 2006.

[12] S. G. Waxman, "Axonal conduction and injury in multiple sclerosis: The role of sodium channels," *Nature Reviews Neuroscience*, vol. 7, pp. 932–941, Dec. 2006.

[13] M. Bär, A. K. Bangia, I. G. Kevrekidis, G. Haas, H.-H. Rotermund, and G. Ertl, "Composite Catalyst Surfaces: Effect of Inert and Active Heterogeneities on Pattern Formation," *The Journal of Physical Chemistry*, vol. 100, pp. 19106–19117, Jan. 1996.

[14] I. Sendiña-Nadal, A. P. Muñuzuri, D. Vives, V. Pérez-Muñuzuri, J. Casademunt, L. Ramírez-Piscina, J. M. Sancho, and F. Sagués, "Wave Propagation in a Medium with Disordered Excitability," *Physical Review Letters*, vol. 80, pp. 5437–5440, June 1998.

[15] O. Steinbock, P. Kettunen, and K. Showalter, "Anisotropy and Spiral Organizing Centers in Patterned Excitable Media," *Science, New Series*, vol. 269, no. 5232, pp. 1857–1860, 1995.

[16] P. Bak, K. Chen, and C. Tang, "A forest-fire model and some thoughts on turbulence," *Physics Letters A*, vol. 147, pp. 297–300, July 1990.

[17] D. W. Zhou, D. D. Mowrey, P. Tang, and Y. Xu, "Percolation Model of Sensory Transmission and Loss of Consciousness Under General Anesthesia," *Physical Review Letters*, vol. 115, p. 108103, Sept. 2015.

[18] D. Stauffer and A. Aharony, *Introduction To Percolation Theory: Second Edition*. London: Taylor & Francis, second ed., Jan. 2017.

[19] A. Aharony, "Universal critical amplitude ratios for percolation," *Physical Review B*, vol. 22, pp. 400–414, July 1980.

[20] A. Seminara, T. E. Angelini, J. N. Wilking, H. Vlamakis, S. Ebrahim, R. Kolter, D. A. Weitz, and M. P. Brenner, "Osmotic spreading of *Bacillus subtilis* biofilms driven by an extracellular matrix," *Proceedings of the National Academy of Sciences*, vol. 109, pp. 1116–1121, Jan. 2012.

[21] H. C. Tuckwell, "Introduction to theoretical neurobiology," 1988.

[22] M. E. Lundberg, E. C. Becker, and S. Choe, "MstX and a Putative Potassium Channel Facilitate Biofilm Formation in Bacillus subtilis," *PLoS ONE*, vol. 8, p. e60993, May 2013.

[23] W. Bialek, A. Cavagna, I. Giardina, T. Mora, O. Pohl, E. Silvestri, M. Viale, and A. M. Walczak, "Social interactions dominate speed control in poising natural flocks near criticality," *Proceedings of the National Academy of Sciences*, vol. 111, pp. 7212–7217, May 2014.

[24] L. Dai, K. S. Korolev, and J. Gore, "Slower recovery in space before collapse of connected populations," *Nature*, vol. 496, pp. 355–358, Apr. 2013.

[25] P. J. Steiner, R. J. Williams, J. Hasty, and L. S. Tsimring, "Criticality and Adaptivity in Enzymatic Networks," *Biophysical Journal*, vol. 111, pp. 1078–1087, Sept. 2016.

[26] T. Mora and W. Bialek, "Are Biological Systems Poised at Criticality?," *Journal of Statistical Physics*, vol. 144, pp. 268–302, July 2011.

[27] I. Irnov and W. C. Winkler, "A regulatory RNA required for antitermination of biofilm and capsular polysaccharide operons in Bacillales: Antitermination of exopolysaccharide genes," *Molecular Microbiology*, vol. 76, pp. 559–575, Mar. 2010.

[28] E. Meijering, O. Dzyubachyk, and I. Smal, "Chapter nine - Methods for Cell and Particle Tracking," in *Methods in Enzymology* (P. M. conn, ed.), vol. 504 of *Imaging and Spectroscopic Analysis of Living Cells*, pp. 183–200, Academic Press, Jan. 2012.

[29] M. Asally, M. Kittisopikul, P. Rue, Y. Du, Z. Hu, T. Cagatay, A. B. Robinson, H. Lu, J. Garcia-Ojalvo, and G. M. Suel, "Localized cell death focuses mechanical forces during 3D patterning in a biofilm," *Proceedings of the National Academy of Sciences*, vol. 109, pp. 18891–18896, Nov. 2012.

[30] J. Humphries, L. Xiong, J. Liu, A. Prindle, F. Yuan, H. A. Arjes, L. Tsimring, and G. M. Süel, "Species-independent attraction to biofilms through electrical signaling," *Cell*, vol. 168, no. 1-2, pp. 200–209.e12, 2017.

[31] M. Huang and C. M. Hull, "Sporulation: How to survive on planet Earth (and beyond)," *Current Genetics*, vol. 63, pp. 831–838, Oct. 2017.

[32] P. Stragier and R. Losick, "Molecular genetics of sporulation in Bacillus subtilis.," *Genetics*, vol. 30, no. 1, pp. 297–341, 1996.

[33] P. J. Piggot and D. W. Hilbert, "Sporulation of Bacillus subtilis," *Current Opinion in Microbiology*, vol. 7, pp. 579–586, Dec. 2004.

[34] R. Pandey, A. Ter Beek, N. O. E. Vischer, J. P. P. M. Smelt, S. Brul, and E. M. M. Manders, "Live Cell Imaging of Germination and Outgrowth of Individual Bacillus subtilis Spores; the Effect of Heat Stress Quantitatively Analyzed with SporeTracker," *PLoS ONE*, vol. 8, p. e58972, Mar. 2013.

[35] S. Wang, P. Setlow, and Y.-q. Li, "Slow Leakage of Ca-Dipicolinic Acid from Individual Bacillus Spores during Initiation of Spore Germination," *Journal of Bacteriology*, vol. 197, pp. 1095–1103, Mar. 2015.

[36] P. Setlow and G. Christie, "Bacterial Spore mRNA – What's Up With That?," *Frontiers in Microbiology*, vol. 11, 2020.

[37] S. Ghosh, G. Korza, M. Maciejewski, and P. Setlow, "Analysis of Metabolism in Dormant Spores of Bacillus Species by 31P Nuclear Magnetic Resonance Analysis of Low-Molecular-Weight Compounds," *Journal of Bacteriology*, vol. 197, pp. 992–1001, Mar. 2015.

[38] S. Wang, J. R. Faeder, P. Setlow, and Y.-q. Li, "Memory of germinant stimuli in bacterial spores," *mBio*, vol. 6, no. 6, pp. e01859–15, 2015.

[39] P. Zhang, J. Liang, X. Yi, P. Setlow, and Y.-q. Li, "Monitoring of Commitment, Blocking, and Continuation of Nutrient Germination of Individual Bacillus subtilis Spores," *Journal of Bacteriology*, vol. 196, pp. 2443–2454, July 2014.

[40] L. V. Pedrero-López, B. Pérez-García, K. Mehltreter, M. E. Sánchez-Coronado, and A. Orozco-Segovia, "Can fern spores develop hydration memory in response to priming?," *Journal of Plant Physiology*, vol. 232, pp. 284–290, Jan. 2019.

[41] N. Brunel and M. C. W. van Rossum, "Lapicque's 1907 paper: From frogs to integrate-and-fire," *Biological Cybernetics*, vol. 97, pp. 337–339, Dec. 2007.

[42] A. N. Burkitt, "A Review of the Integrate-and-fire Neuron Model: I. Homogeneous Synaptic Input," *Biological Cybernetics*, vol. 95, pp. 1–19, July 2006.

[43] P. Setlow, "Germination of Spores of Bacillus Species: What We Know and Do Not Know," *Journal of Bacteriology*, vol. 196, pp. 1297–1305, Apr. 2014.

[44] A. Moir and G. Cooper, "Spore Germination," *Microbiology Spectrum*, vol. 3, Dec. 2015.

[45] J. W. Larkin, X. Zhai, K. Kikuchi, S. E. Redford, A. Prindle, J. Liu, S. Greenfield, A. M. Walczak, J. Garcia-Ojalvo, A. Mugler, and G. M. Süel, "Signal Percolation within a Bacterial Community," *Cell Systems*, vol. 7, pp. 137–145.e3, Aug. 2018.

[46] C.-Y. Yang, M. Bialecka-Fornal, C. Weatherwax, J. W. Larkin, A. Prindle, J. Liu, J. Garcia-Ojalvo, and G. M. Süel, "Encoding Membrane-Potential-Based Memory within a Microbial Community," *Cell Systems*, vol. 10, pp. 417–423.e3, May 2020.

[47] T. Sirec, J. M. Benarroch, P. Buffard, J. Garcia-Ojalvo, and M. Asally, "Electrical polarization enables integrative quality control during bacterial differentiation into spores.," *iScience*, vol. 16, pp. 378–389, 2019.

[48] A. L. Hodgkin and A. F. Huxley, "A quantitative description of membrane current and its application to conduction and excitation in nerve," *The Journal of Physiology*, vol. 117, pp. 500–544, Aug. 1952.

[49] E. Eisenstadt, "Potassium Content During Growth and Sporulation in Bacillus subtilis," *Journal of Bacteriology*, vol. 112, no. 1, pp. 264–267, 1972.

[50] A. M. Whatmore, J. A. Chudek, and R. H. . Reed, "The effects of osmotic upshock on the intracellular solute pools of Bacillus subtilis," *Microbiology*, vol. 136, no. 12, pp. 2527–2535.

[51] L. Zheng, W. Abhyankar, N. Ouwerling, H. L. Dekker, H. van Veen, N. N. van der Wel, W. Roseboom, L. J. de Koning, S. Brul, and C. G. de Koster, "Bacillus subtilis Spore Inner Membrane Proteome," *Journal of Proteome Research*, vol. 15, pp. 585–594, Feb. 2016.

[52] G. Holtmann, E. P. Bakker, N. Uozumi, and E. Bremer, "KtrAB and KtrCD: Two K+ Uptake Systems in Bacillus subtilis and Their Role in Adaptation to Hypertonicity," *J. BACTERIOL.*, vol. 185, p. 10, 2003.

[53] J. Stautz, Y. Hellmich, M. F. Fuss, J. M. Silberberg, J. R. Devlin, R. B. Stockbridge, and I. Hänelt, "Molecular Mechanisms for Bacterial Potassium Homeostasis," *Journal of Molecular Biology*, p. 166968, Mar. 2021.

[54] J. Barfield, C. Yeung, and T. Cooper, "Characterization of potassium channels involved in volume regulation of human spermatozoa," *Molecular Human Reproduction*, vol. 11, pp. 891–897, Dec. 2005.

[55] D. E. Cortezzo, B. Setlow, and P. Setlow, "Analysis of the action of compounds that inhibit the germination of spores of Bacillus species," *Journal of Applied Microbiology*, p. 17, 2004.

[56] E. Mancilla and E. Rojas, "Quinine blocks the high conductance, calcium-activated potassium channel in rat pancreatic β-cells," *FEBS Letters*, vol. 260, pp. 105–108, Jan. 1990.

[57] C. Mitchell, J. Skomurski, and J. Vary, "Effect of ion channel blockers on germination of Bacillus megaterium spores," *FEMS Microbiology Letters*, vol. 34, pp. 211–214, Apr. 1986.

[58] D.-y. D. Lee, L. Galera-Laporta, M. Bialecka-Fornal, E. Moon, Z. Shen, S. P. Briggs, J. Garcia-Ojalvo, and G. M. Süel, "Magnesium flux modulates ribosomes to increase bacterial survival," *Cell*, 2019.

[59] A. E. Cowan, E. M. Olivastro, D. E. Koppel, C. A. Loshon, B. Setlow, and P. Setlow, "Lipids in the inner membrane of dormant spores of Bacillus species are largely immobile," *Proceedings of the National Academy of Sciences*, vol. 101, pp. 7733–7738, May 2004.

[60] A. P. Leonard, R. B. Cameron, J. L. Speiser, B. J. Wolf, Y. K. Peterson, R. G. Schnellmann, C. C. Beeson, and B. Rohrer, "Quantitative analysis of mitochondrial morphology and membrane potential in living cells using high-content imaging, machine learning, and morphological binning," *Biochimica et Biophysica Acta*, p. 13, 1853.

[61] A. Perez-Valdespino, Y. Li, B. Setlow, S. Ghosh, D. Pan, G. Korza, F. E. Feeherry, C. J. Doona, Y.-Q. Li, B. Hao, and P. Setlow, "Function of the SpoVAEa and SpoVAF Proteins of Bacillus subtilis Spores," *Journal of Bacteriology*, vol. 196, pp. 2077–2088, June 2014.

[62] H. Jarmer, R. Berka, S. Knudsen, and H. H. Saxild, "Transcriptome analysis documents induced competence of *Bacillus subtilis* during nitrogen limiting conditions," *FEMS Microbiology Letters*, vol. 206, pp. 197–200, Jan. 2002.

[63] J. M. Sterlini and J. Mandelstam, "Commitment to sporulation in Bacillus subtilis and its relationship to development of actinomycin resistance," *Biochemical Journal*, vol. 113, pp. 29–37, June 1969.

[64] S. Atluri, K. Ragkousi, D. E. Cortezzo, and P. Setlow, "Cooperativity Between Different Nutrient Receptors in Germination of Spores of Bacillus subtilis and Reduction of This Cooperativity by Alterations in the GerB Receptor," *Journal of Bacteriology*, vol. 188, pp. 28–36, Jan. 2006.

[65] L. Sinai, A. Rosenberg, Y. Smith, E. Segev, and S. Ben-Yehuda, "The Molecular Timeline of a Reviving Bacterial Spore," *Molecular Cell*, vol. 57, pp. 695–707, Feb. 2015.

[66] P. S. Rana, B. A. Gibbons, A. A. Vereninov, V. E. Yurinskaya, R. J. Clements, T. A. Model, and M. A. Model, "Calibration and characterization of intracellular Asante Potassium Green probes, APG-2 and APG-4," *Analytical Biochemistry*, vol. 567, pp. 8–13, Feb. 2019.

[67] D. L. Garmaise, G. Y. Paris, J. Komlossy, C. H. Chambers, and R. C. McCrae, "Anthelmintic quaternary salts. III. Benzothiazolium salts," *Journal of Medicinal Chemistry*, vol. 12, pp. 30–36, Jan. 1969.

[68] A. Dey and A. Hajra, "Metal-Free Synthesis of 2-Arylbenzothiazoles from Aldehydes, Amines, and Thiocyanate," *Organic Letters*, vol. 21, pp. 1686–1689, Mar. 2019.

[69] C. S. Ra, B. Y. Jung, and G. Park, "The fungicidal benzothiazole methoxyacrylates: Synthesis, conformational analysis and fungicidal activity.," *Heterocycles*, vol. 62, pp. 793–802, 2004.

[70] M. Seelam, B. V. Shaikh, R. Tamminana, and P. R. Kammela, "An efficient methodology for the synthesis of thioureas from amine mediated by a cobalt source," *Tetrahedron Letters*, vol. 57, pp. 5297–5300, Nov. 2016.

[71] H. Inoue, M. Konda, T. Hashiyama, H. Otsuka, A. Watanabe, M. Gaino, K. Takahashi, T. Date, K. Okamura, M. Takeda, H. Narita, S. Murata, A. Odawara, H. Sasaki, and T. Nagao, "Synthesis and biological evaluation of alkyl, alkoxy, alkylthio, or amino-substituted 2,3-dihydro-1,5-benzothiazepin-4(5H)-ones," *Chemical & Pharmaceutical Bulletin*, vol. 45, pp. 1008–1026, June 1997.

[72] S. Tzanopoulou, M. Sagnou, M. Paravatou-Petsotas, E. Gourni, G. Loudos, S. Xanthopoulos, D. Lafkas, H. Kiaris, A. Varvarigou, I. C. Pirmettis, M. Papadopoulos, and M. Pelecanou, "Evaluation of Re and ^{99m} Tc Complexes of 2-(4′-Aminophenyl)benzothiazole as Potential Breast Cancer Radiopharmaceuticals," *Journal of Medicinal Chemistry*, vol. 53, pp. 4633–4641, June 2010.

[73] M. Chhabra, S. Sinha, S. Banerjee, and P. Paira, "An efficient green synthesis of 2-arylbenzothiazole analogues as potent antibacterial and anticancer agents," *Bioorganic & Medicinal Chemistry Letters*, vol. 26, pp. 213–217, Jan. 2016.